Saddle-point finder and its application to the spin foam model

Zichang Huang,[1,2,*] Shan Huang,[1,2] and Yidun Wan[1,2,3,†]

[1]State Key Laboratory of Surface Physics, Department of Physics, Center for Field Theory and Particle Physics, and Institute for Nanoelectronic devices and Quantum computing, Fudan University, Shanghai 200433, China

[2]Shanghai Qi Zhi Institute, Shanghai 200030, China

[3]Zhangjiang Fudan International Innovation Center, Fudan University, Shanghai 201210, China

(Received 20 July 2022; accepted 23 January 2023; published 22 February 2023)

We introduce a saddle-point finder that can find the complex saddle points for any analytically continued action. We showcase our saddle-point finder by two examples in the EPRL spin foam model: the single vertex case and the case of triangulation Δ_3. In both cases, the complex saddle points are found, and each saddle point's contribution to the partition function is estimated. We also discuss the geometrical interpretation of each saddle point.

DOI: 10.1103/PhysRevD.107.046011

I. INTRODUCTION

Witten has suggested using complex path integral to study the physical theories with complex-valued couplings [1–3]. Later, Refs. [4–12] have related complex path integrals to the sign problem in the Euclidean path integral of QCD and models with finite chemical potential. Works on supersymmetric theories [13–16] pointed out that the complex saddle points related to the bions are important to provide the right vacuum energy. Even for theories with real couplings, complexifying the path integrals is always necessary [17].

In loop quantum gravity [18–20], a recent result [21] has shown that the key to solving the long-existing flatness problem [22–26] is to find the complex saddle points of the analytically continued Engle-Pereira-Rovelli-Livine (EPRL) spin foam action [27,28]. These complex saddle points dominate the whole path integral when curvature exists; they are also categorized and endowed with geometrical interpretations [29]. Another recent result [30] has used the Lefschetz thimbles attached to the complex saddle points as the integral cycles to numerically compute the correlation functions in the spin foam model. As such, studying the properties of the complex saddle points is necessary in a wide range of physical theories.

For a complicated action, e.g., the spin foam action, solving the saddle point equation analytically can hardly be possible. This paper thus develops a numerical saddle-point finder that possesses the following characters[1]:

(1) working for complex valued action,
(2) being able to find saddle points without analytically solving the saddle point equation, and
(3) being able to estimate the contribution of each saddle point to the partition function.

To work for complexified path integrals, our saddle-point finder combines the generalized thimble method (GTM) [31] and a perturbative saddle-point finder (PSPF). The GTM uses the Lefschetz thimbles as integral cycles in a path integral to suppress the oscillation of the integrand in the complex-valued action. On Lefschetz thimbles, the GTM samples points by the distribution $e^{S_{\text{eff}}}$, where the effective action S_{eff} sums the real part of the action S and the logarithm of the real part of the Jacobian caused by the deformation of the integral cycle. Sampled points with significant statistical weights should be close to and thus can roughly locate the saddle points of S. At a sampled point, our PSPF finds where the local minimal value of $|\partial_\mu S|$ can be taken. Therefore, PSPF pins the saddle points around the sampled points. After finding the saddle points, one can compute the real part of the action at each of these saddle points to estimate its contribution to the whole partition function.

The method used in [21] only applies to the cases of small deficit angles. Yet, there lacks an explicit relation between the real saddle points in the case of zero deficit angles and the complex saddle points in the cases of arbitrary deficit angles. As mentioned in [21,32,33], figuring out the spin foam's asymptotic behavior, which is influenced by the complex saddle points, is vital to the renormalization procedure of the spinfoam. To renormalize the spin foam to check the semiclassical consistency and to explore the behavior of the spin foam in different discretization schemes, finding the complex saddle points in spin foams is important.

*hzc881126@hotmail.com
†ydwan@fudan.edu.cn

[1]The saddle point method only applies to nondegenerate saddle points where the determinant of the Hessian is not zero. This paper considers nondegenerate saddle points only.

In this paper, we showcase our saddle-point finder by two examples in the EPRL spin foam model: the single vertex case and the case of triangulation Δ_3. our finder can find multiple complex saddle points in the large deficit angle case. Furthermore, we find that in the large deficit angle case, multiple complex saddle points contribute to the spin foam amplitude and list these saddle points by their contributions to the partition function.

The paper is organized as follows. Section II reviews the GTM. Section III introduces our saddle-point finder. Section IV reviews the analytically continued spin foam model. Sections V and VI apply our saddle-point finder to the single-vertex EPRL spin foam and Δ_3-triangulated EPRL spin foam. Finally, Sec. VII concludes the paper.

II. LEFSCHETZ THIMBLE

A Lefschetz thimble is a multidimensional generalization of the stationary phase contour of a single-variable complex function. References [1,3] use the thimble method to define a new type of partition functions as integrals over thimbles instead of over $\mathbb{R}^N$. Thimble method is also used in the asymptotic analysis related to the resurgent trans-series [34]. Numerically, the thimble method is used to compute observables when the action is complex valued ([31,35–41] etc.). For us, the thimble method can help roughly estimate the positions of saddle points.

One of the most important properties of the thimbles is that the imaginary part of the action is a constant on each thimble. Therefore, the path integral along thimbles is not oscillatory. Assuming a complex valued action S of a lattice model, one of the most useful integrals in the path integral formulation reads

$$F = \int \mathrm{d}^N x O(\mathbf{x}) \mathrm{e}^{-S(\mathbf{x})}. \tag{1}$$

When O is 1, F is the partition function. To apply the thimble method, one has to first assume that $O(\mathbf{x})$ and $S(\mathbf{x})$ can be analytically continued as the holomorphic functions $\hat{O}(\mathbf{z})$ and $\hat{S}(\mathbf{z})$, such that

$$F = \int_{\mathbb{R}^N} \mathrm{d}^N z \hat{O}(\mathbf{z}) \mathrm{e}^{-\hat{S}(\mathbf{z})}. \tag{2}$$

The Picard-Lefschetz theory shows that the integral can be equivalently decomposed into a linear combination of integrals over N-dimensional integral cycles $\mathcal{J}_\sigma, \sigma = 1 \cdots N$:

$$F = \sum_\sigma n_\sigma \int_{\mathcal{J}_\sigma} \mathrm{d}^N z \hat{O}(\mathbf{z}) \mathrm{e}^{-\hat{S}(\mathbf{z})}, \tag{3}$$

where $\mathcal{J}_\sigma$ labels the Lefschetz thimbles, and n_σ labels the weight of each thimble. Each thimble $\mathcal{J}_\sigma$ is defined as a union of the steepest decent (SD) paths meeting two conditions:

(1) Each path $z(t)$ is a solution to the SD equation

$$\frac{\mathrm{d}z^a}{\mathrm{d}t} = -\frac{\partial \overline{\hat{S}(\mathbf{z})}}{\partial \overline{z^a}}, \tag{4}$$

where z^a are the coordinates of the point $\mathbf{z}(t)$.

(2) On each path, $\mathbf{z}(t)$ goes to a saddle point $\mathbf{p}_\sigma$ when $t \to \infty$.

Because

$$\frac{\mathrm{d}\hat{S}}{\mathrm{d}t} = \frac{\partial \hat{S}}{\partial z^a}\frac{\mathrm{d}z^a}{\mathrm{d}t} = -\left|\frac{\partial \hat{S}}{\partial z^a}\right|^2, \tag{5}$$

$\mathrm{Re}(\hat{S})$ monotonically decreases along each SD path and approaches its minimum at the saddle point[2]; $\mathrm{Im}(\hat{S})$ is conserved along each SD path. Therefore, on each thimble, the phase of each integrand becomes a constant, and

$$\int_{\mathcal{J}_\sigma} \mathrm{d}^N z \hat{O}(\mathbf{z}) \mathrm{e}^{-\hat{S}(\mathbf{z})} = \mathrm{e}^{-\mathrm{iIm}(\hat{S}(p_\sigma))} \int_{\mathcal{J}_\sigma} \mathrm{d}^N z \hat{O}(\mathbf{z}) \mathrm{e}^{-\mathrm{Re}(\hat{S}(\mathbf{z}))}, \tag{6}$$

where the factor $\mathrm{e}^{-\mathrm{Re}(\hat{S}(\mathbf{z}))}$ is nonoscillatory now. As a result, the oscillatory integral F is equivalent to a combination of certain nonoscillatory integrals.

One thing to remark here is that $\hat{O}$ and $\hat{S}$ may be meromorphic. Equation (3) does not work when extra poles are brought in by the analytically continuation. Therefore, the thimble method may not work under this situation. Later in this section we will show that the GTM can be applied in the case when $\hat{S}$ is meromorphic and $\hat{O}$ is holomorphic. But, because the $\hat{O}$ does not affect the saddle point value of the $\hat{S}$, GTM is capable of finding the saddle points.

In some simple cases when only one thimble dominates the whole path integral, the thimble method can be easily applied in computing observables. An observable $\langle O \rangle$ reads

$$\langle O \rangle = \frac{\int \mathrm{d}^N x O(\mathbf{x}) \mathrm{e}^{-S(\mathbf{x})}}{\int \mathrm{d}^N x \mathrm{e}^{-S(\mathbf{x})}}. \tag{7}$$

By the thimble method,

[2]Remark that even though one reaches the saddle point by decreasing the real part of the action, the saddle point on the Lefschetz thimble is in fact a maximum of the real part of the action on the Lefschetz thimble.

$$\langle O\rangle = \frac{\int \mathrm{d}^N z \hat{O}(\mathbf{z}) \mathrm{e}^{-\hat{S}(\mathbf{z})}}{\int \mathrm{d}^N z \mathrm{e}^{-\hat{S}(\mathbf{z})}} = \frac{\sum_\sigma n_\sigma \mathrm{e}^{-\mathrm{iIm}(\hat{S}(p_\sigma))} \int_{\mathcal{J}_\sigma} \mathrm{d}^N z \hat{O}(\mathbf{z}) \mathrm{e}^{-\mathrm{Re}(\hat{S}(\mathbf{z}))}}{\sum_\sigma n_\sigma \mathrm{e}^{-\mathrm{iIm}(\hat{S}(p_\sigma))} \int_{\mathcal{J}_\sigma} \mathrm{d}^N z \mathrm{e}^{-\mathrm{Re}(\hat{S}(\mathbf{z}))}} \tag{8}$$

if $\hat{O}$ and $\hat{S}$ are holomorphic. Assuming the thimble $\mathcal{J}_{\sigma'}$ governs the whole integral, $\langle O\rangle$ becomes

$$\langle O\rangle = \frac{\int_{\mathcal{J}_{\sigma'}} \mathrm{d}^N z \hat{O}(\mathbf{z}) \mathrm{e}^{-\mathrm{Re}(\hat{S}(\mathbf{z}))}}{\int_{\mathcal{J}_{\sigma'}} \mathrm{d}^N z \mathrm{e}^{-\mathrm{Re}(\hat{S}(\mathbf{z}))}}, \tag{9}$$

whose nominator and denominator are both nonoscillatory integrals. In this case, the Lefschetz thimble method turns an oscillatory path integral into a statistical-mechanics problem. In fact, $\int_{\mathcal{J}_{\sigma'}} \mathrm{d}^N z \mathrm{e}^{-\mathrm{Re}(\hat{S}(\mathbf{z}))}$ shown in (9) is a partition function denoted as Z, where $\mathrm{e}^{-\mathrm{Re}(\hat{S}(\mathbf{z}))}$ can be considered as a Boltzmann factor. Such a statistical-mechanical system can be simulated by the Markov chain Monte Carlo (MCMC) method that samples points on the thimble $\mathcal{J}_{\sigma'}$ by the distribution $\mathrm{e}^{-\mathrm{Re}(\hat{S}(\mathbf{z}))}/Z$, and $\langle O\rangle$ is the mean value of $\hat{O}(\mathbf{z})$ among these sampled points. Note that $\mathrm{Re}(S)$ decreases along the SD paths, so the point possessing the largest $\mathrm{e}^{-\mathrm{Re}(\hat{S}(\mathbf{z}))}$ on $\mathcal{J}_{\sigma'}$ should be the saddle point $\mathbf{p}_{\sigma'}$. Thus, most sampled points should cluster around the saddle point.

In general cases when multiple thimbles contribute to the integral, the previous way to compute $\langle O\rangle$ is practically hard to realize because

(1) multiple thimbles contribute non-negligibly to $\langle O\rangle$,
(2) and it is impossible to find the thimbles by solving the SD equation (4) with $t \to \infty$ in computers.

Therefore, GTM has been developed to do the computation. Instead of using the SD equation, GTM uses the steepest ascend (SA) equation

$$\frac{\mathrm{d}z^a}{\mathrm{d}t} = \overline{\frac{\partial \hat{S}(\mathbf{z})}{\partial \bar{z}^a}} \tag{10}$$

to approach the thimbles. Let $\mathbf{z}(t)$ be a solution to (10) and $\mathbf{x} = \mathbf{z}(0)$. Define $\mathcal{F}_T(\mathbf{x}) \coloneqq \mathbf{z}(T)$. An N-dimensional manifold $\mathcal{M}_T$ can be defined as $\{\mathcal{F}_T(\mathbf{x})|\mathbf{x} \in \mathbb{R}^N\}$. By Cauchy's theorem,

$$F = \int_{\mathbb{R}^N} \mathrm{d}^N z \hat{O}(\mathbf{z}) \mathrm{e}^{-\hat{S}(\mathbf{z})} = \int_{\mathcal{M}_T} \mathrm{d}^N z \hat{O}(z) \mathrm{e}^{-\hat{S}(\mathbf{z})}, \tag{11}$$

where the deformation from $\mathcal{M}_0 = \mathbb{R}^N$ to $\mathcal{M}_T$ is continues. According to [31], in the limit $T \to \infty$, $\mathcal{M}_{T\to\infty} = \sum_\sigma n_\sigma \mathcal{J}_\sigma$. Therefore, for a large enough T,

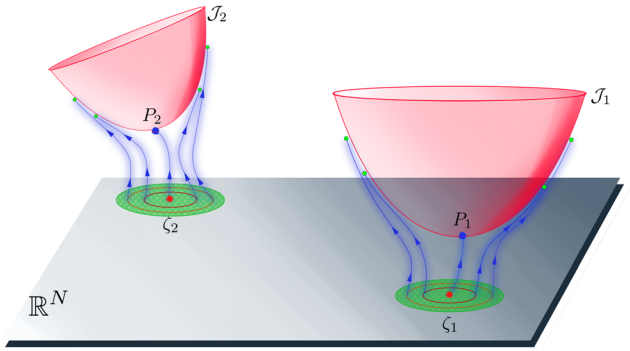

FIG. 1. The gray plate indicates $\mathbb{R}^N$ and the red manifolds $\mathcal{J}_1$ and $\mathcal{J}_2$ are two Lefschetz thimbles. The blue arrows indicate the SA flow. By SA flow, ζ_1 and ζ_2 are mapped to the saddle points ζ_1 and ζ_2, and the points in the green disks around ζ_1 and ζ_2 are mapped to the points close to the corresponding thimbles.

$$F = \sum_\sigma n_\sigma \int_{\mathcal{J}_\sigma} \mathrm{d}^N z \hat{O}(\mathbf{z}) \mathrm{e}^{-\hat{S}(\mathbf{z})} \sim \int_{\mathcal{M}_T} \mathrm{d}^N z \hat{O}(\mathbf{z}) \mathrm{e}^{-\hat{S}(\mathbf{z})}. \tag{12}$$

For some scattered points $\zeta \in \mathbb{R}^N$, $\mathcal{F}_T(\zeta)$ approach the saddle points $\mathbf{P}_\sigma$ of the thimbles with nonzero n_σ; for the points $\mathbf{x} \in \mathbb{R}^N$ close to ζ, the set of $\mathcal{F}_T(\mathbf{x})$ forms an N-dimensional manifold approaching to the combination of $\mathcal{J}_\sigma$ (Fig. 1). To compute $\int_{\mathcal{M}_T} \mathrm{d}^N z \hat{O}(\mathbf{z}) \mathrm{e}^{-\hat{S}(\mathbf{z})}$, we label each point $\mathcal{F}_T(\mathbf{x}) \in \mathcal{M}_T$ by its initial point $x \in \mathbb{R}^N$ and transform $\int_{\mathcal{M}_T}$ back to $\int_{\mathbb{R}^N}$.

Consider $\mathbb{R}^N = \mathcal{M}_0$, when $T = 0$, $\partial \mathcal{F}_0(\mathbf{x})^k / \partial x^i = \delta_i^k$ defines the coordinate transformation from $\mathbb{R}^N$ to $\mathcal{M}_0$, and $\det \delta = 1$ is the Jacobian for this coordinate transformation. When $T \neq 0$, the evolution of $\partial \mathcal{F}_t(\mathbf{x})^k / \partial x^i$ along an SA path is governed by

$$\frac{\mathrm{d}(\partial \mathcal{F}_t(\mathbf{x})^k / \partial x^i)}{\mathrm{d}t} = \sum_{l=1}^{n} \overline{\frac{\partial^2 \hat{S}(\mathcal{F}_t(\mathbf{x}))}{\partial \mathcal{F}_t(\mathbf{x})^k \partial \mathcal{F}_t(\mathbf{x})^l}} \left(\overline{\partial \mathcal{F}_t(\mathbf{x})^l / \partial x^i}\right). \tag{13}$$

With the initial condition $\partial \mathcal{F}_0(\mathbf{x})^k / \partial x^i = \delta_i^k$, (13) has the solution $\partial \mathcal{F}_T(\mathbf{x})^k / \partial x^i$, which describes the coordinate transformation from $\mathcal{F}_T(\zeta)$ to ζ, with the Jacobian $J_T(\mathbf{x}) = \det(\partial \mathcal{F}_T(\mathbf{x})^k / \partial x^i)$. As such, (12) becomes

$$F \sim \int_{\mathcal{M}_T} \mathrm{d}^N z \hat{O}(\mathbf{z}) \mathrm{e}^{-\hat{S}(\mathbf{z})} = \int_{\mathbb{R}^N} \mathrm{d}^N x J_T(\mathbf{x}) \hat{O}(\mathcal{F}_T(\mathbf{x})) \mathrm{e}^{-\hat{S}(\mathcal{F}_T(\mathbf{x}))}. \tag{14}$$

Let $S_{T\mathrm{eff}} = \mathrm{Re}(\hat{S}) - \log(\det(J_T))$ be the purely real effective action and $\theta_{T\mathrm{res}} = \arg(\det(J_T)) - \mathrm{Im}(\hat{S})$ be the residual phase, (14) becomes

$$F \sim \int_{\mathbb{R}^N} \mathrm{d}^N x \hat{O}(\mathcal{F}_T(\mathbf{x})) \mathrm{e}^{\mathrm{i}\theta_{T\mathrm{res}}} \mathrm{e}^{-S_{T\mathrm{eff}}(\mathcal{F}_T(\mathbf{x}))}, \quad (15)$$

where $\mathrm{e}^{-S_{T\mathrm{eff}}(\mathcal{F}_T(\mathbf{x}))}$ can be considered as the Boltzmann factor of a sampling process on $\mathbb{R}^N$. The observable (9) can be computed by the reweighted method [31]:

$$\begin{aligned}\langle O \rangle &\sim \frac{\int_{\mathbb{R}^N} \mathrm{d}^N x \hat{O}(\mathcal{F}_T(\mathbf{x})) \mathrm{e}^{\mathrm{i}\theta_{T\mathrm{res}}} \mathrm{e}^{-S_{T\mathrm{eff}}(\mathcal{F}_T(\mathbf{x}))}}{\int_{\mathbb{R}^N} \mathrm{d}^N x \mathrm{e}^{\mathrm{i}\theta_{T\mathrm{res}}} \mathrm{e}^{-S_{T\mathrm{eff}}(\mathcal{F}_T(\mathbf{x}))}}, \\ &= \frac{\int_{\mathbb{R}^N} \mathrm{d}^N x \hat{O}(\mathcal{F}_T(\mathbf{x})) \mathrm{e}^{\mathrm{i}\theta_{T\mathrm{res}}} \mathrm{e}^{-S_{T\mathrm{eff}}(\mathcal{F}_T(\mathbf{x}))}}{\int_{\mathbb{R}^N} \mathrm{d}^N x \mathrm{e}^{-S_{T\mathrm{eff}}(\mathcal{F}_T(\mathbf{x}))}} \\ &\quad \times \frac{\int_{\mathbb{R}^N} \mathrm{d}^N x \mathrm{e}^{-S_{T\mathrm{eff}}(\mathcal{F}_T(\mathbf{x}))}}{\int_{\mathbb{R}^N} \mathrm{d}^N x \mathrm{e}^{\mathrm{i}\theta_{T\mathrm{res}}} \mathrm{e}^{-S_{T\mathrm{eff}}(\mathcal{F}_T(\mathbf{x}))}}, \\ &= \frac{\langle \hat{O} \mathrm{e}^{\mathrm{i}\theta_{T\mathrm{res}}} \rangle_{T\mathrm{eff}}}{\langle \mathrm{e}^{\mathrm{i}\theta_{T\mathrm{res}}} \rangle_{T\mathrm{eff}}}. \end{aligned} \quad (16)$$

$\langle f \rangle_{T\mathrm{eff}}$ is the mean value of any given f among the sampled points.

Although the integrands in (16) are still oscillatory, the fluctuation is much smaller in $\mathcal{M}_T$ than in $\mathbb{R}^N$ for large T. In $\mathcal{M}_T$, the points with significant distribution come from small isolated regions around the saddle points. In each such small region, $\mathrm{e}^{\mathrm{i}\theta_{T\mathrm{res}}}$ oscillates mildly. Outside these small regions, $\mathrm{e}^{\mathrm{i}\theta_{T\mathrm{res}}}$ oscillates severely, but the points here contribute little to the whole integral. As a result, the larger T is, the smaller the contributing regions are and the less oscillating the integrands are. This property ensures that with a properly chosen T, most the sampled points in the GTM are around the saddle points, and our saddle-point finder uses this fact.

Besides, the choice of T is important in the GTM. On the one hand, large T can suppress the oscillation of the integrands. On the other hand, the larger the T, the more isolated the contributing regions. Isolated regions are a landscape that is hard to be sampled by samplers like MCMC or slice sampling. For a multimodal distribution with multiple contributing regions, the sampler depending on local movements may be trapped in one of the regions. To resolve this issue, the world-volume-tempered Lefschetz thimble method (WV-TLTM) has been developed [42]. By Cauchy's theorem, the value of $\langle O \rangle$ is independent of the choice of T:

$$\langle O \rangle \sim \frac{\langle \hat{O} \mathrm{e}^{\mathrm{i}\theta_{T_1\mathrm{res}}} \rangle_{T_1\mathrm{eff}}}{\langle \mathrm{e}^{\mathrm{i}\theta_{T_1\mathrm{res}}} \rangle_{T_1\mathrm{eff}}} = \frac{\langle \hat{O} \mathrm{e}^{\mathrm{i}\theta_{T_2\mathrm{res}}} \rangle_{T_2\mathrm{eff}}}{\langle \mathrm{e}^{\mathrm{i}\theta_{T_2\mathrm{res}}} \rangle_{T_2\mathrm{eff}}}, \qquad T_1 \neq T_2. \quad (17)$$

Therefore, $\langle O \rangle$ can be computed by considering the contributions of different T, i.e.,

$$\langle O \rangle \sim \frac{\int_{T_0}^{T_1} \mathrm{d}T \mathrm{e}^{-W(T)} \int_{\mathbb{R}^N} \mathrm{d}^N x \hat{O}(\mathcal{F}_T(\mathbf{x})) \mathrm{e}^{\mathrm{i}\theta_{T\mathrm{res}}} \mathrm{e}^{-S_{T\mathrm{eff}}(\mathcal{F}_T(\mathbf{x}))}}{\int_{T_0}^{T_1} \mathrm{d}T \mathrm{e}^{-W(T)} \int_{\mathbb{R}^N} \mathrm{d}^N x \mathrm{e}^{\mathrm{i}\theta_{T\mathrm{res}}} \mathrm{e}^{-S_{T\mathrm{eff}}(\mathcal{F}_T(\mathbf{x}))}}, \quad (18)$$

where $W(T)$ is an arbitrary function. In this computation, the sampling is performed on the world volume defined as

$$\mathcal{R} = \bigcup_{i=T_0}^{T_1} \mathcal{M}_T.$$

In an $\mathcal{M}_T$ with small T, the contributing regions are so large that they will contact with each other, and the sampler may use this $\mathcal{M}_T$ as a bridge between the isolated regions in large T slices. Therefore, by considering the interval between a small T and a large T, WV-TLTM can sample over all the regions containing saddle points.

III. SADDLE-POINT FINDER

In our finder, saddle points are found by a two-level searching procedure. On the first level, the GTM serves as the coarse finder to roughly locate the saddle points. On the second level, the PSPF is deployed to pin the saddle points. This section introduces the coarse finder first and then the pinpoint finder.

A. The coarse finder

The GTM can sample the points around saddle points. Specifically, we use the ensemble slice sampling method [43] as the sampler and WV-TLTM to combine the contributions of the different evolution time T. The finder consists of the following steps:

(1) Choose A points $\{\mathbf{x}_i, i = 1 \cdots A\}$. If the action is a function depending on N complex variables, $A > 2N$ is suggested.
(2) Using $\{\mathbf{x}_i, i = 1 \cdots A\}$ as initial points of the SA flow, find the maximal time T_1, till which the differential equation solver can evolve all these points. Pick a time $T_0 < T_1$ and use (T_0, T_1) as the time interval in WV-TLTM.
(3) Apply the ensemble slice sampling method (Algorithm 1) to sample on the world volume by the distribution density $\mathrm{e}^{-S_{T\mathrm{eff}}(\mathcal{F}_T(\mathbf{x}))}$.
(4) Sort the sampled points x by their effective action. Take the first P points as the output of the finder. Here, P is a parameter of the finder, and it needs to be tuned to achieve the best performance.

In the second step, any ordinary differential equation (ODE) solver cannot evolve the SA flow for infinitely long. The right-hand side of (10) becomes larger and larger when the flow is leaving the saddle point. The ODE numerical solvers, e.g., Runge-Kutta, Rosenbrock, etc, use difference equations to approximate the differential equations. The error of this approximation is proportional to the norm of the

Algorithm 1. Ensemble slice sampling.

Given t, f, S:
Initialize $N_e^{(t)} = 0$ and $N_c^{(t)} = 0$
for $k = 1, \ldots, A$ **do**
  Get direction vector $\vec{\eta}_k$
  Sample $Y \sim \text{Uniform}(0, f(\mathbf{x}_k^{(t)}))$
  Sample $U \sim \text{Uniform}(0, 1)$
  Set $L \leftarrow -U$, and $R \leftarrow L + 1$
  while $Y < f(\mathbf{x}_k^{(t)} + L\vec{\eta}_k)$ **do**
    $L \leftarrow L - 1$
    $N_e^{(t)} \leftarrow N_e^{(t)} + 1$
  end while
  while $Y < f(\mathbf{x}_k^{(t)} + R\vec{\eta}_k)$ **do**
    $R \leftarrow R + 1$
    $N_e^{(t)} \leftarrow N_e^{(t)} + 1$
  end while
  while True **do**
    Sample $X' \sim \text{Uniform}(L, R)$
    Set $Y' \leftarrow f(X'\vec{\eta}_k + \mathbf{x}_k^{(t)})$
    if $Y < Y'$ **then**
      break
    end if
    if $X' < 0$ **then**
      $L \leftarrow X'$
      $N_c^{(t)} \leftarrow N_c^{(t)} + 1$
    else
      $R \leftarrow X'$
      $N_c^{(t)} \leftarrow N_c^{(t)} + 1$
    end if
  end while
  Set $\mathbf{x}_k^{(t+1)} \leftarrow X'\eta_k + \mathbf{x}_k^{(t)}$
end for

right-hand side of the differential equations. Therefore, the error increases with the evolution time, and the maximal time T_1 is the largest evolution time, such that the error is under the given tolerance.

The ensemble slice sampling (ESS) used in the third step is a powerful MCMC sampler that applies to complicated cases. As a type of slice sampling [44], the basic idea of ESS is that sampling from a distribution $p(x)$ whose density is proportional to $f(x)$ is equivalent to uniformly sampling from the region below the curve of $f(x)$. In many cases [43], ESS performs better than those random-walking based MCMC sampler for multimodal distribution, and we take this advantage of ESS to sample on the $\mathcal{M}_T$. The ESS defines an ensemble $\{\mathbf{x}_1, \cdots \mathbf{x}_A\}$ of parallel chains and generates moves by the positions of the current head of the chains $\{\mathbf{x}_1^{(t)}, \cdots \mathbf{x}_A^{(t)}\}$. In each ESS iteration, we first apply the differential move scheme to generate the direction vector for each chain $\mathbf{x}_k$. This scheme comprises two steps:

(1) From the complementary ensemble $S_{[k]} = \{\mathbf{x}_n, \forall\ n \neq k\}$, draw two chains $\mathbf{x}_l$ and $\mathbf{x}_m$ uniformly and without replacement.
(2) Compute the direction vector $\vec{\eta}_k$ by $\vec{\eta}_k = \mu(\mathbf{x}_l - \mathbf{x}_m)$.

The parameter μ can be automatically tuned by the method in [43]. Then, we apply $\vec{\eta}_k$ in Algorithm 1 to generate the moves for this ESS iteration. The whole ESS sampling process consists of multiple ESS iterations.

In our work, the distribution $f(\mathbf{x})$ is chosen to be $e^{-S_{T\text{eff}}(\mathcal{F}_T(\mathbf{x}))}$, and the space for sampling is $\mathbb{R}^N$. We remark that although theoretically the ergodicity of WV-TLTM is proven, the efficiency of the sampling procedure can be very low for a large N. We can improve the efficiency of the finder with the following pretreatments:

(1) Find a compact region of interest as the working place of the finder.
(2) Find the points with small value of $|\partial_\mu f(\mathbf{x})|$ within the compact region by physical facts or by optimization algorithm, e.g., annealing algorithm, genetic algorithm, particle swarm algorithm, etc. Use those points the initial points.

B. The pinpoint finder

The MCMC sampler cannot exactly sample saddle point. Most samples are located near the saddle points. Thus, we develops a pinpoint finder to nail down the saddle points. The coarse finder feeds multiple points around the saddle points to the pinpoint finder that applies the PSPF to locate the saddle points. The PSPF is based on that there always exists a point $\tilde{x}$ such that $|\partial_\mu f(\tilde{x})| \leq |\partial_\mu f(x)|$ for any $x \in \mathbb{C}^N$ and a locally smooth function $f(x)$ with $\det \frac{\partial^2 f(x)}{\partial x^\mu \partial x^\nu} \neq 0$. Let $\vec{\epsilon} = -(\frac{\partial^2 f(x)}{\partial x^\mu \partial x^\nu})^{-1} \partial_\nu f(x)$, $\partial_\mu f(x + \alpha\epsilon)$ expands as

$$\begin{aligned}\partial_\mu f(x+\alpha\epsilon) &= \partial_\mu f(x) + \alpha \frac{\partial^2 f(x)}{\partial x^\mu \partial x^\nu}\epsilon^\nu + O(\alpha^2\epsilon^2), \\ &= \partial_\mu f(x) - \alpha \frac{\partial^2 f(x)}{\partial x^\mu \partial x^\nu}\left(\frac{\partial^2 f(x)}{\partial x^\nu \partial x^\lambda}\right)^{-1}\partial_\lambda f(x) \\ &\quad + O(\alpha^2\epsilon^2), \\ &= (1-\alpha)\partial_\mu f(x) + O(\alpha^2\epsilon^2). \end{aligned} \tag{19}$$

Hence, for a positive but sufficiently small α, $|\partial_\mu f(x + \alpha\epsilon)| < |\partial_\mu f(x)|$, then we can use $x + \alpha\epsilon$ as the $\tilde{x}$. Recursively taking the output $\tilde{x}$ as the input x, one can find the location of the nearest local minimal value of $|\partial_\mu f|$ where $\det \frac{\partial^2 f(x)}{\partial x^\mu \partial x^\nu} \neq 0$. Algorithm 2 with three parameters (N, toa, tol) summarizes the PSPF method.

The parameter N defines the upper limit of the number of iterations; toa and tol are the lower bounds of α and $|\alpha\epsilon|$; toa indicates the accuracy of the algorithm. The algorithm terminates when the PSPF finds $||f(x_0)| - |f(\tilde{x})|| < tol$. For a point far away from all the saddle points [Fig. 2(b)], the PSPF cannot find the saddle points. Nevertheless, when a point is close to one of the saddle points [Fig. 2(a)] the PSPF can find saddle points. Consequently, pinpoint finder can locate the saddle points from most points fed by the coarse finder.

Algorithm 2. Perturbative Finder.

Given parameters N, toa, and tol and function f:
Initialise $k = 0$
while $k < N$ **do**
  $\varepsilon \leftarrow -(f''(x_0))^{-1} \cdot f'(x_0)$
  $\alpha \leftarrow 0$
  while $\alpha < toa$ **do**
    $C \leftarrow |f'(x_0)| - |f'(x_0 + 10^{-\alpha} \times \varepsilon)|$
    if $C > 0$ **then**
      break
    end if
    $\alpha \leftarrow \alpha + 1$
  end while
  if $C < tol$ **then**
    break
  end if
  $x_0 \leftarrow x_0 + 10^{-\alpha} \times \varepsilon$
  $k \leftarrow k + 1$
end while

C. Additional instructions

Our coarse finder is based on ESS, which is a type of MCMC. Similar to many of MCMC programs, e.g., CosmoMC, CoBaya, PyMC, etc. ([45,46] etc.), we suggest to find a compact region of interest as the working place of the finder as a pre-treatment to improve the efficiency. The ergodicity of ESS is proven in [43] for N-dimensional cases if the number of the Markov chains is greater than $2N$. The [43] also shows that the average time of each sampling step reaches its minimum when the number of threads running in the computer is equal to half of the number of the Markov chains. Therefore, the typical dimension of the problem to apply our coarse finder should be equal to or smaller than the number of threads that computer can efficiently run in parallel. In order to converge to the target distribution, ESS has to run for a large number of steps. Although there is no prediction on the exact value of this large number, one can always use Gelman-Rubin diagnostic to see whether the program runs long enough to converge (see Appendix D for details).

Our pinpoint finder can only work for the cases with $\det \frac{\partial^2 f(x)}{\partial x^\mu \partial x^\nu} \neq 0$. Therefore, the finder can only find nondegenerate saddle points. In fact, in the Lefschetz thimble method, thimbles attach only to nondegenerate saddle points, and degenerate saddle points do not contribute to the partition function. The benchmark of the pinpoint is given in Appendix E. Our benchmark shows that the pinpoint finder uses $\mathcal{O}(N^2)$ time to find the saddle points in N-dimensional cases. Thus, our pinpoint finder is ran by a polynomial algorithm and should be applicable in any finite dimensional cases.

Finally, we admit that our saddle-point finder may miss some of the nondegenerate saddle points. In general, the pinpoint finder will not be fed by all the samples from the coarse finder. After the Markov chains converge, we let ESS continue to sample K points and choose initial points of the pinpoint finder from these K points. Thus, some of the saddle points may be neglected. One can increase the K to let pinpoint finder find more saddle points or fed all the sampled points to the pinpoint finder to find all the saddle point in a very long time. Besides, though some of the saddle points are missing at certain values of K, the remaining saddle points include the most contributing ones.

IV. THE ANALYTICALLY CONTINUED SPIN FOAM MODEL

Spin foam is a covariant formulation of loop quantum gravity [27,47–50]. In this work, we use the EPRL spin foam model [27] to test our saddle-point finder. Here, we review the action of the EPRL spin foam model, the analytic continuation of the EPRL action, the classification of the complex saddle points of the analytically continued action, and the classical limit of the spin foam model.

Loop quantum gravity aims to quantize the pseudo-Riemannian geometry to describe quantum spacetimes. In loop quantum gravity, quantized three-dimensional spaces are spin-network states [51,52]. The evolution of spin-network states constructs quantum spacetimes. Geometric variables in pseduo-Riemannian geometry are promoted as

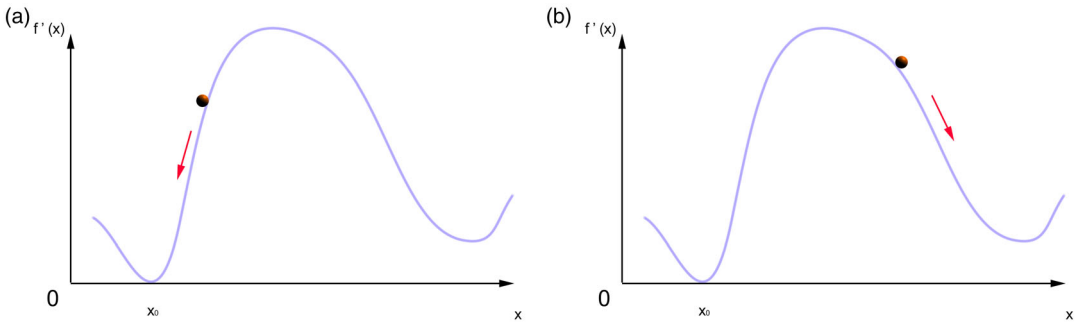

FIG. 2. For both figures, the vertical axis corresponds to the $f'(x)$ and the horizontal axis corresponds to the x. For (a), the red point is close to the saddle point x_0, and PSPF can move the red points to x_0. For (b), there is a bump between the saddle point x_0 and the red point, and PSPF cannot move the red point to the saddle point.

quantum operators. Following the spin-geometry theorem proposed by Penrose [53], spin-network states can be considered as a "polymeric foam" made by combining multiple "quanta of the space." In the simplicial case, each "quantum of the space" is a quantum tetrahedron, which is a tensor state consisting of four angular momentum states satisfying the condition

$$(\hat{\mathbf{J}}^{(1)}+\hat{\mathbf{J}}^{(2)}+\hat{\mathbf{J}}^{(3)}+\hat{\mathbf{J}}^{(4)})|\psi\rangle=0, \tag{20}$$

where $\hat{\mathbf{J}}^{(i)}$ are the angular momentum operators. Each of these angular momentum states is a face of the quantum tetrahedron, and $\hat{\mathbf{J}}^{(i)}$ is proportional to the normal operator of the face. Condition (20) is a quantum version of the closure condition of a classical tetrahedron. In loop quantum gravity, the quantum space time is the evolution from one spin-network state to another. The spin foam theory provides a way to compute the transition amplitude—the spin foam amplitude—of this evolution and hence the expectation values of geometric-variable operators. For example, three-dimensional metric is promoted as the Penrose metric operator, and its connected correlation function is related to the graviton propagator [54–60]. Usually, evolution of a spin-network state has a basic building block called a vertex in spin foam theory. A vertex describes the evolution involving five quantum tetrahedra (m initial and $5-m$ finial quantum tetrahedra). The tensor state of m initial and $5-m$ finial quantum tetrahedra makes a boundary state [61,62]. Spin foam theory provides the transition amplitude of each vertex by summing over all the bulk degrees of freedom. In the EPRL model, the spin foam amplitude of a vertex is given by

$$Z=\int_{SL(2,\mathbb{C})^5}\prod_a \mathrm{d}g_a\prod_{a>b}P_{ab}(g), \tag{21}$$

where

$$P_{ab}(g)=\langle j_{ab},-\vec{n}_{ab}|Y^\dagger g_a^{-1}g_b Y|j_{ba},\vec{n}_{ba}\rangle. \tag{22}$$

Here, the Latin indices a and b label the five quantum tetrahedra. For each P_{ab}, the states $|j_{ba},\vec{n}_{ba}\rangle$ and $|j_{ab},\vec{n}_{ab}\rangle$ stand for a pair of faces evolving to each other. The operator Y maps the spin-j $SU(2)$ irreducible representation $\mathcal{H}_j$ to the lowest level in $SL(2,\mathbb{C})$ $(j,\gamma j)$-irreducible representation $\mathcal{H}_{(j,\gamma j)}=\oplus_{k=j}^{\infty}\mathcal{H}_k$. Here, γ is the Barbero-Immirzi parameter,[3] $g_a\in SL(2,\mathbb{C})$ embeds the face $Y|j_{ba},\vec{n}_{ba}\rangle$ in four dimensions. Therefore, each P_{ab} stands for the amplitude when faces $|j_{ba},\vec{n}_{ba}\rangle$ and $|j_{ab},\vec{n}_{ab}\rangle$ coincide in four dimensions. The integral of the bulk degrees of freedom $\int_{SL(2,\mathbb{C})^5}\prod_a \mathrm{d}g_a$ traverses all the possible embeddings, and Z is the transition amplitude when the five tetrahedra interact with each other. Since the elements in $\mathcal{H}_{(j,\gamma j)}$ can be expressed as homogeneous functions on $\mathbb{CP}_1$, the inner product (22) is equivalent to the integral [63,64]

$$\begin{aligned}P_{ab}=\frac{d_{j_{ab}}}{\pi}\int_{\mathbb{CP}^1}\mathrm{d}\tilde{\mathbf{z}}_{ab}\langle Z_{ba},Z_{ba}\rangle^{-(1-\mathrm{i}\gamma)j_{ab}}\langle Z_{ab},Z_{ab}\rangle^{-(1+\mathrm{i}\gamma)j_{ab}}\\ \times\langle\xi_{ab},Z_{ab}\rangle^{2j_{ab}}\langle Z_{ba},\xi_{ba}\rangle^{2j_{ab}},\end{aligned} \tag{23}$$

in which $d_j=2j+1$, $Z_{ab}=g_a^\dagger z_{ab}$, and $Z_{ba}=g_h^\dagger z_{ab}$. The integral measure $\mathrm{d}\tilde{\mathbf{z}}_{ab}=-(\langle Z_{ab},Z_{ab}\rangle\langle Z_{ba},Z_{ba}\rangle)^{-1}\mathrm{d}\mathbf{z}_{ab}$ (with $\mathrm{d}\mathbf{z}=\frac{i}{2}(z_0dz_1-z_1dz_0)\wedge(\bar{z}_0d\bar{z}_1-\bar{z}_1d\bar{z}_0)$) is homogeneous on $\mathbb{CP}^1$. The bracket $\langle\cdot,\cdot\rangle$ is the SU(2)-invariant inner product. Using this expression, the spin foam amplitude in this simple case reads

$$Z=\int_{SL(2,\mathbb{C})^5}\prod_a \mathrm{d}g_a\int\left(\prod_{a>b}\frac{d_{j_{ab}}}{\pi}\mathrm{d}\tilde{\mathbf{z}}_{ab}\right)\mathrm{e}^S, \tag{24}$$

with

$$\begin{aligned}S(j,g,\mathbf{z})=\sum_{a>b}[&2j_{ab}\log(\langle\xi_{ab},Z_{ab}\rangle\langle Z_{ba},\xi_{ba}\rangle)\\ &-(1+\mathrm{i}\gamma)j_{ab}\log\langle Z_{ab},Z_{ab}\rangle\\ &-(1-\mathrm{i}\gamma)j_{ab}\log\langle Z_{ba},Z_{ba}\rangle].\end{aligned} \tag{25}$$

In the general, multiple vertices exist. Similar to the single-vertex case, the general form of the spin foam amplitude on a simplicial complex $\mathcal{K}$ reads

$$Z=\sum_{\vec{j}}\prod_f\mathbf{d}_{J_f}\int[\mathrm{d}X]\mathrm{e}^{\sum_f J_f F_f[X,T]}, \tag{26}$$

where f labels the 2-faces in $\mathcal{K}$ colored by spins J_f, $\sum_{\vec{j}}$ means summing over all the possible ways of coloring $\mathcal{K}$ by spins, X collects all the variables to be integrated, T collects the parameters determined by the given boundary state, and $\sum_f J_f F_f[X,T]$ is the action.

In the Lorentzian EPRL model,

$$\begin{cases}\mathbf{d}_{J_f}=2J_f+1\\ X\equiv(g_{ve},z_{vf},\xi^I_{ef})\\ \mathrm{d}X\equiv\mathrm{d}g_{ve}\mathrm{d}\tilde{z}_{vf}\mathrm{d}\xi^I_{ef}\\ T\equiv(\xi^B_{ef})\end{cases}. \tag{27}$$

Here, v denotes a 4-simplex in $\mathcal{K}$, and each three-dimensional tetrahedron in ∂v is denoted by e. For each v, the group variables $g_{ve}\in\mathrm{SL}(2,\mathbb{C})$ are assigned to tetrahedra; the spinor variables $z_{vf}\in\mathbb{CP}^1$ are assigned to the faces (see Fig. 3). Both ξ^I_{ef} and ξ^B_{ef} are $\mathbb{C}^2$ spinors normalized by

[3]In loop quantum gravity, the physical area of a face is given by $A_{phy}=8\pi\hbar G\gamma\sqrt{j(j+1)}$, where j is the spin of the face state. Therefore, $8\pi\hbar G\gamma$ defines a physical units of the area spectrum.

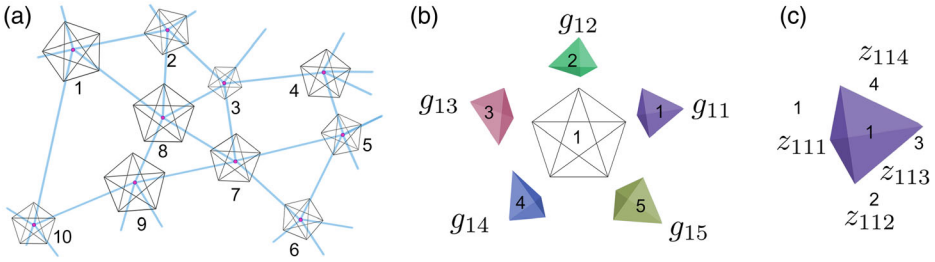

FIG. 3. (a) In a simplical complex, the 4-simplices are labeled by v, $v = 1, \ldots, 10$. (b) For 4-simplex 1, five tetrahedra are labeled by e, $e = 1, \ldots, 5$. Each tetrahedron is assigned with a group variable g_{ve}, where ve is 12, 13, 14, 15. (c) For the tetrahedron $ve = 11$, the faces are labeled by 111, 112, 113, 114, and each face is assigned by a spinor.

Hermitian inner product. Variables ξ^I_{ef}, which are assigned to the internal faces in $\mathcal{K}$, need to be integrated. Parameters ξ^B_{ef}, which are assigned to the boundary faces, are fixed by the boundary states. The $\mathrm{SL}(2,\mathbb{C})$ Haar measure $\mathrm{d}g_{ve}$ can be expressed as [65]

$$\mathrm{d}g = \frac{\mathrm{d}\beta\mathrm{d}\beta^*\mathrm{d}\gamma\mathrm{d}\gamma^*\mathrm{d}\delta\mathrm{d}\delta^*}{|\delta|^2} \quad \forall\ g = \begin{pmatrix} \alpha & \beta \\ \gamma & \delta \end{pmatrix}. \tag{28}$$

Let $Z_{vef} = g^\dagger_{ve} z_{vf}$ and $\langle\cdot,\cdot\rangle$ be the SU(2) invariant inner product, $\forall\, z_{vf} = (z_0, z_1)$,

$$\begin{aligned} \mathrm{d}\tilde{z}_{vf} &= -\frac{\mathrm{d}z_{vf}}{\langle Z_{vef}, Z_{vef}\rangle\langle Z_{ve'f}, Z_{ve'f}\rangle}, \\ &= -\frac{i}{2}\frac{(z_0\mathrm{d}z_1 - z_1\mathrm{d}z_0)\wedge(\bar{z}_0 d\bar{z}_1 - \bar{z}_1 d\bar{z}_0)}{\langle Z_{vef}, Z_{vef}\rangle\langle Z_{ve'f}, Z_{ve'f}\rangle}. \end{aligned} \tag{29}$$

Here, $e, e' \in \partial v$ are two tetrahedra sharing the face f. Let $\{v | f \subset v\}$ as the set of 4-simplices containing the face f,

$$\begin{aligned} F_f[X,T] = \sum_{\{v|f\subset v\}} \Bigg(&\ln\frac{\langle \xi_{ef}, Z_{vef}\rangle^2\langle Z_{ve'f}, \xi_{e'f}\rangle^2}{\langle Z_{vef}, Z_{vef}\rangle\langle Z_{ve'f}, Z_{ve'f}\rangle} \\ &- i\gamma \ln\frac{\langle Z_{vef}, Z_{vef}\rangle}{\langle Z_{ve'f}, Z_{ve'f}\rangle}\Bigg), \end{aligned} \tag{30}$$

where γ is the Barbero-Immirzi parameter. Depending on $\mathcal{K}$, ξ_{ef} can be either ξ^I_{ef} or ξ^B_{ef}. By the convention in [28,65–67], some of the ξ_{ef} in F_f can be replaced by $J\xi_{ef}$ where $J\xi = (\bar{\xi}_2, -\bar{\xi}_1)$ for a spinor $\xi = (\xi_1, \xi_2)$.

The EPRL spin foam action has two types of gauge degrees of freedom—the continuous gauges and the discrete gauge [65]. There are three continuous gauge degrees of freedom:

(1) Rescaling of z_{vf}:

$$z_{vf} \mapsto \lambda z_{vf}, \qquad \lambda \in \mathbb{C}. \tag{31}$$

(2) $\mathrm{SL}(2,\mathbb{C})$ gauge transformation at each 4-simplex v:

$$g_{ve} \mapsto x_v^{-1} g_{ve}, \quad z_{vf} \mapsto x_v^\dagger z_{vf}, \quad x_v \in \mathrm{SL}(2,\mathbb{C}). \tag{32}$$

(3) SU(2) gauge transformation on each internal tetrahedron e, i.e., the tetrahedron shared by two 4-simplices:

$$g_{ve} \mapsto g_{ve} h_e^{-1}, \qquad h_e \in \mathrm{SU}(2). \tag{33}$$

The discrete gauge is flipping the sign of the group variables $g_{ve} \mapsto -g_{ve}$. The group variables take value of Lorentz group $\mathrm{SO}^+(1,3)$ rather than its double-cover $\mathrm{SL}(2,\mathbb{C})$.

In our work, we parametrize the EPRL spin foam action after fixing the continuous gauges. By fixing the rescaling gauge of z_{vf}, each z_{vf} can be parametrized by two real variables:

$$z_{vf} = (1, x_{vf} + \mathrm{i}y_{vf}). \tag{34}$$

By fixing the $\mathrm{SL}(2,\mathbb{C})$ gauge in each 4-simplex, one can set one of the five g_{ve} at each vertex v as identity. For any $\mathrm{SL}(2,\mathbb{C})$ group element g, one can always decompose g into $g'h$ where h is an SU(2) element and g' is a triangular matrix. Thus, to fix the SU(2) gauge in the internal tetrahedron e, one can parametrize one of two $\mathrm{SL}(2,\mathbb{C})$ elements assigned to e as

$$\begin{pmatrix} \lambda^{-1} & x + \mathrm{i}y \\ 0 & \lambda \end{pmatrix}, \qquad \lambda \in \mathbb{R}\backslash\{0\}, x, y \in \mathbb{R} \tag{35}$$

and parametrize the other $\mathrm{SL}(2,\mathbb{C})$ element as

$$\begin{pmatrix} 1 + (x_1 + \mathrm{i}y_1)/\sqrt{2} & (x_2 + \mathrm{i}y_2)/\sqrt{2} \\ (x_3 + \mathrm{i}y_3)/\sqrt{2} & \frac{1+(x_2+\mathrm{i}y_2)(x_3+\mathrm{i}y_3)/2}{1+(x_1+\mathrm{i}y_1)/\sqrt{2}} \end{pmatrix}, \quad \times\, x_1, y_1, x_2, y_2, x_3, y_3 \in \mathbb{R}. \tag{36}$$

For each boundary tetrahedron, the assigned $\mathrm{SL}(2,\mathbb{C})$ element is also parametrized as (36) too.

It is convenient to shift one of the saddle points to the origin $x = y = 0$.[4] Denoting $(1, z_{0vf})$ and g_{0ve} as the saddle point value of z_{vf} and g_{ve}, (34)–(36) can be modified as

$$\begin{aligned} z_{vf} &= (1, z_{0vf} + x_{vf} + \mathrm{i}y_{vf}), \\ g_{ve} &= g_{0ve}\begin{pmatrix} \lambda^{-1} & x+\mathrm{i}y \\ 0 & \lambda \end{pmatrix}, \\ g_{ve} &= g_{0ve}\begin{pmatrix} 1+(x_1+\mathrm{i}y_1)/\sqrt{2} & (x_2+\mathrm{i}y_2)/\sqrt{2} \\ (x_3+\mathrm{i}y_3)/\sqrt{2} & \frac{1+(x_2+\mathrm{i}y_2)(x_3+\mathrm{i}y_3)/2}{1+(x_1+\mathrm{i}y_1)/\sqrt{2}} \end{pmatrix}. \end{aligned} \tag{37}$$

With the parametrization defined by (34)–(36), the measure $\mathrm{d}g_{ve}$ and $\mathrm{d}z_{vf}$ become

$$\begin{aligned} dg &= \frac{1}{128\pi^4}\frac{dx_1dx_2dx_3dy_1dy_2dy_3}{|1+\frac{x_1+\mathrm{i}y_1}{\sqrt{2}}|^2}, \\ \mathrm{d}z_{vf} &= \mathrm{d}x_{vf}\mathrm{d}y_{vf}. \end{aligned}$$

The analytic continuation of F_f can be realized by complexifing the group variables g_{ve} and the spinor variables z_{vf}. After this complexification, $g_{ve} \in \mathrm{SL}(2,\mathbb{C})$ becomes $\tilde{g}_{ve} \in SO(4,\mathbb{C})$, and $g^{\dagger}_{ve} \in \mathrm{SL}(2,\mathbb{C})$ becomes $\tilde{g}'_{ve} \in SO(4,\mathbb{C})$, which is independent of $\tilde{g}_{ve}$. Similarly, the spinor $z_{vf} \in \mathbb{CP}^1$ becomes $\tilde{z}_{vf} \in \mathbb{C}^2$, and $\bar{z}_{vf}$ becomes $\tilde{z}'_{vf} \in \mathbb{C}^2$, which is independent of $\tilde{z}_{vf}$. This analytic continuation complexifies all the real parameters appearing in (34)–(36).

From the saddle points of the analytic continued EPRL spin foam action, one can reconstruct a pair of bivectors $B^{\pm}_{vef}$. Let Z^0_{vef} be the saddle point value, the spinor representations of the bivectors are

$$B^{+}_{vef} = \chi_{vef} \otimes \bar{Z}^{0\prime}_{vef} - \frac{1}{2}\mathbf{1}, \tag{38}$$

$$B^{-}_{vef} = \bar{Z}^{0}_{vef} \otimes \chi'_{vef} - \frac{1}{2}\mathbf{1}. \tag{39}$$

When vef is a boundary face, χ'_{vef} and χ_{vef} read

$$\begin{aligned} \chi'_{vef} &= \frac{\mathrm{i}\gamma+\kappa_{vef}}{\mathrm{i}\gamma-1}\frac{\bar{Z}^{0\prime}_{vef}}{\bar{Z}^{0\prime}_{vef}\bar{Z}^{0}_{vef}} - \frac{\kappa_{vef}+1}{\mathrm{i}\gamma-1}\frac{\xi^{\dagger}_{vef}}{\xi^{\dagger}_{vef}\bar{Z}^{0}_{vef}}, \\ \chi_{vef} &= \frac{\mathrm{i}\gamma+\kappa_{vef}}{\mathrm{i}\gamma+1}\frac{\bar{Z}^{0}_{vef}}{\bar{Z}^{0\prime}_{vef}\bar{Z}^{0}_{vef}} - \frac{\kappa_{vef}-1}{\mathrm{i}\gamma+1}\frac{\xi_{vef}}{\bar{Z}^{0\prime}_{vef}\xi_{vef}}. \end{aligned} \tag{40}$$

When vef is a bulk face,

$$\begin{aligned} \chi'_{vef} &= \frac{\mathrm{i}\gamma+\kappa_{vef}}{\mathrm{i}\gamma-1}\frac{\bar{Z}^{0\prime}_{vef}}{\bar{Z}^{0\prime}_{vef}\bar{Z}^{0}_{vef}} - \frac{\kappa_{vef}+1}{\mathrm{i}\gamma-1}\frac{\bar{Z}^{0\prime}{}_{vef}}{\bar{Z}^{0\prime}{}_{vef}\bar{Z}^{0}_{vef}}, \\ \chi_{vef} &= \frac{\mathrm{i}\gamma+\kappa_{vef}}{\mathrm{i}\gamma+1}\frac{\bar{Z}^{0}_{vef}}{\bar{Z}^{0\prime}_{vef}\bar{Z}^{0}_{vef}} - \frac{\kappa_{vef}-1}{\mathrm{i}\gamma+1}\frac{\bar{Z}^{0}_{vef}}{\bar{Z}^{0\prime}_{vef}\bar{Z}^{0}_{vef}}. \end{aligned} \tag{41}$$

The $\kappa_{vef} = \pm 1$ depends on the orientation. The four-dimensional bivectors are given by the spin-1 representation of $B_{\pm vef}$. At each vertex the bivectors $B^{IJ}_{\pm vef}$ are classified into the following three types corresponding to different geometries.

(1) Nondegenerate simplicial geometry: The bivectors at the vertex indicates a 4-simplex. Each of the 10 faces is represented by a bivector B^f. For each tetrahedron, the bivectors of the four faces satisfy the closure condition:

$$\sum_{j,j\neq i} B^f_{ij} = 0. \tag{42}$$

The volume V_i of tetrahedron i is nonzero. Each tetrahedron has a four-dimensional normal vector N^i:

$$N^i B^f_{ij} = 0. \tag{43}$$

This condition is also known as the cross simplicial condition [68]. The four-dimensional normal vectors fulfill the four-dimensional closure condition:

$$\sum_i V_i N_i = \sum_i U_i = 0. \tag{44}$$

The volume of the 4-simplex is nonzero:

$$v_a = \frac{5!}{\sum_{ijkl}\epsilon_{ijkl}\det[U_i, U_j, U_k, U_l]} \neq 0. \tag{45}$$

(2) Degenerate vector geometry: The bivectors at the vertex are interpreted as the vector geometry. There exist 10 bivectors corresponding to 10 faces, and they all belong to the same three-dimensional subspace. For each tetrahedron, the closure condition and cross simplicial condition hold; however, the four-dimensional normal vectors of the five tetrahedra are parallel to each other. Therefore, the volume of v is ill-defined, rendering this type of geometry degenerate.

(3) Lorentzian $SO(1,3)$ bivector geometry: This type of geometry also depends on 10 faces represented by bivectors. These bivectors fulfill the closure condition but not the cross simplicial condition. This indicates that those 10 faces cannot form five tetrahedra as required by the simplicial geometry.

This classification depends crucially on the behavior of the four-dimensional normal vectors. At each saddle point, one

[4]Here, x and y stand for all real variables in (36), (35), and (34).

can always try to reconstruct the four-dimensional normal vectors by $\tilde{g}_{ve}$, $\tilde{g}'_{ve}$, $\tilde{z}_{vf}$, and $\tilde{z}'_{vf}$. If the four-dimensional normal vectors at a saddle point cannot be reconstructed, the saddle point indicates an $SO(1,3)$ bivector geometry. If the reconstructed normal vectors at a saddle point are parallel to each other, then the saddle point indicates a vector geometry, and if they make $\epsilon_{ijkl}\det[U_i,U_j,U_k,U_l]$ nonzero, the saddle point indicates a simplicial geometry.

In spin foam theory, there are three important limits: semiclassical limit, refinement limit, and the classical limit. In the semiclassical limit $j\to\infty$, the saddle points dominate the spin foam amplitudes ([50,64,66,67,69,70] etc.). A general belief [50] is that the saddle points corresponding to the simplicial geometry contribute far more than other types of saddle points. Therefore, in semiclassical limit, the EPRL model, flow to the Regge geometry, i.e., a discrete version of general relativity. In refinement limit, the number of the vertices goes to infinity, and the EPRL model should flow to a continuous theory of quantum gravity. Classical limit combines the semiclassical limit and the refinement limit. In this limit, the EPRL model reproduces general relativity. There are many ways of combining semiclassical and refinement limits. One such way [55,71] suggests to increase j and the number of vertices simultaneously while keeping the deficit angle on each triangle face small. Since any Riemannian geometry without singularity can be approximated by a Regge geometry containing sufficiently many 4-simplices with sufficiently small deficit angles, this way of taking the limit can drive the EPRL model to general relativity.

V. APPLICATION: THE SADDLE POINTS IN THE SINGLE 4-SIMPLEX SPIN FOAM MODEL

A. The action

The first example of applying our saddle point finder is the single-vertex spin foam model. This model describes how five spacelike quantum tetrahedra interact with each other. In this model, we only have one 4-simplex, so we can neglect the v label in this section. The index a labels the tetrahedra, and the index pair ab labels the face shared by two tetrahedra a and b. The index a runs from 1 to 5 because a 4-simplex has five boundary tetrahedra. All the faces in a 4-simplex are boundary faces, whose geometric information is encoded in the parameters ξ_{ab}. Following [57–60], we use a coherent spin-network state as the boundary state, such that (26) takes the form

$$Z=\sum_{\vec{J}}\psi_{J_0,\zeta_0}\prod_{ab}\mathbf{d}_{J_{ab}}\int[\mathrm{d}X]\mathrm{e}^{\sum_{a>b}J_{ab}F_{ab}[X,T]}. \tag{46}$$

In this section, we have

$$\begin{cases}\mathbf{d}_{J_{ab}}=2J_{ab}+1\\ X\equiv(g_a,z_{ab},J_{ab})\\ \mathrm{d}X\equiv(\mathrm{d}g_a,\mathrm{d}\tilde{z}_{ab})\\ T\equiv(\xi_{ab},\zeta_0^{ab},J_{0ab},\alpha^{(ab)(cd)})\end{cases}, \tag{47}$$

$$\psi_{J_0,\zeta_0}=\exp\left(-i\sum_{ab}\zeta_0^{ab}(J_{ab}-J_{0ab})\right)\times\exp\left(-\sum_{ab,cd}\alpha^{(ab)(cd)}\frac{J_{ab}-J_{0ab}}{\sqrt{J_{0ab}}}\frac{J_{cd}-J_{0cd}}{\sqrt{J_{0cd}}}\right), \tag{48}$$

and

$$F_{ab}=[2\log(\langle J\xi_{ab},Z_{ab}\rangle\langle Z_{ba},\xi_{ba}\rangle)-(1+\mathrm{i}\gamma)\log\langle Z_{ab},Z_{ab}\rangle-(1-\mathrm{i}\gamma)\log\langle Z_{ba},Z_{ba}\rangle],\quad a>b. \tag{49}$$

Here, $Z_{ab}=g_a^\dagger z_{ab}$; ξ_{ab}, ζ_0^{ab}, J_{0ab}, and $\alpha^{(ab)(cd)}$ are the parameters given by the boundary state; g_a and z_{ab} are variables to be integrated; J_{ab} are spin variables to be summed up. In addition, we introduce a scale factor λ, such that $J_{ab}=\lambda j_{ab}$, $J_{0ab}=\lambda j_{0ab}$.

We adopt the 4-simplex geometry used in [21,30,72] to generate the boundary state. The five vertices of this 4-simplex are

$$\begin{aligned}&P_1=(0,0,0,0),\qquad P_2=(0,0,0,-2\sqrt{5}/3^{1/4}),\\ &P_3=(0,0,-3^{1/4}\sqrt{5},-3^{1/4}\sqrt{5}),\\ &P_4=(0,-2\sqrt{10}/3^{3/4},-\sqrt{5}/3^{3/4},-\sqrt{5}/3^{1/4}),\\ &P_5=(-3^{-1/4}10^{-1/2},-\sqrt{5/2}/3^{3/4},-\sqrt{5}/3^{3/4},-\sqrt{5}/3^{1/4}).\end{aligned}$$

Then, the 4-normal vectors of the tetrahedra are

$$\begin{aligned}&N_1=(-1,0,0,0),\qquad N_2=\left(\frac{5}{\sqrt{22}},\sqrt{\frac{3}{22}},0,0\right),\\ &N_3=\left(\frac{5}{\sqrt{22}},-\frac{1}{\sqrt{66}},\frac{2}{\sqrt{33}},0\right),\\ &N_4=\left(\frac{5}{\sqrt{22}},-\frac{1}{\sqrt{66}},-\frac{1}{\sqrt{33}},\frac{1}{\sqrt{11}}\right),\\ &N_5=\left(\frac{5}{\sqrt{22}},-\frac{1}{\sqrt{66}},-\frac{1}{\sqrt{33}},-\frac{1}{\sqrt{11}}\right).\end{aligned} \tag{50}$$

Table I lists all the ten j_0 s. The spinors ξ_{ba} and $J\xi_{ab}$ are related to the 3-normal vectors $\vec{n}_{ba}$ and $-\vec{n}_{ab}$, respectively by $\vec{n}_{ba}=\langle\xi_{ba}|\vec{\sigma}|\xi_{ba}\rangle$ and $-\vec{n}_{ab}=\langle J\xi_{ab}|\vec{\sigma}|J\xi_{ab}\rangle$. Table II (III) records all the 3-normal (4-normal) vectors of the 4-simplex.

The matrix $\alpha^{(ab)(cd)}$ must have a positive definite real part, and

TABLE I. Each cell shows the area of the face shared by line number tetrahedra and column number tetrahedra.

	b			
	j_{0ab}			
a	2	3	4	5
1	5	5	5	5
2	⋯	2	2	2
3	⋯	⋯	2	2
4	⋯	⋯	⋯	2

$$\alpha^{(ab)(cd)} = \alpha_1 P_0^{(ab)(cd)} + \alpha_2 P_1^{(ab)(cd)} + \alpha_3 P_2^{(ab)(cd)},$$

where α_1, α_2, α_3 are free parameters. The basis $P_k^{(ab)(cd)}(k = 0\ldots2)$ are defined as

(1) $P_0^{(ab)(cd)} = 1$ if $(ab) = (cd)$ and zero otherwise.
(2) $P_1^{(ab)(cd)} = 1$ if $a = c$, $b \neq d$ and zero otherwise.
(3) $P_2^{(ab)(cd)} = 1$ if $(ab) \neq (cd)$ and zero otherwise.

In this paper, we set $\alpha_1 = 7.8816/\gamma$, $\alpha_2 = 0.1224/\gamma$, and $\alpha_3 = 1.4814/\gamma$. The choice of α does not affect the application of our algorithm.

The parameters ζ_0^{ab}, whose values are given in Table IV, are related to the dihedral angles between the 4-normal vectors (50). One can find the way to determine ζ_0^{ab} in [30].

By Poisson resummation, the summation $\sum_{a>b}$ can be approximated by the integral $\int dj$ [30] when the λ is large. Thus, the action and the partition function read

$$S_{\text{tot}} = \mathrm{i}\lambda \sum_{ab} \zeta_0^{ab}(j_{ab} - j_{0ab}) + \lambda \sum_{ab,cd} \alpha^{(ab)(cd)} \frac{j_{ab} - j_{0ab}}{\sqrt{j_{0ab}}} \times \frac{j_{cd} - j_{0cd}}{\sqrt{j_{0cd}}} - \sum_{a>b} \lambda j_{ab} F_{ab}, \tag{51}$$

and

$$Z = \int \prod_a \mathrm{d}g_a \prod_{a>b} \mathrm{d}j_{ab} \mathrm{d}\tilde{z}_{ab} \mathbf{d}_{\lambda j_{ab}} \mathrm{e}^{S_{\text{tot}}}, \tag{52}$$

which has the same form as (1).

In our computation, we set $\gamma = 0.1$ and $\lambda = 50$.

B. Pretreatments

To apply our saddle point finder, we apply the following pretreatments:

(1) Fix the $\mathrm{SL}(2,\mathbb{C})$ gauge by fixing g_1 to be identity.
(2) Parameterize the variables g_a, j_{ab}, and z_{ab}. In the single 4-simplex case, all the tetrahedra are boundary tetrahedra. We parametrize g_2 to g_5 as in (36). Each j_{ab} is a real variable. z_{ab} are parametrized in the form (34). Hence, the total action depends on 54 real variables.
(3) The works [30,57–60,73] pointed out that the action (51) has a saddle point s_0 with geometric interpretation. At the saddle point s_0, $j_{ab} = j_{0ab}$, and Table V (VI) records the values of g_a (z_{ab}).

TABLE II. Each cell shows the three-dimensional normal vector of the face shared by line number tetrahedra and column number tetrahedra.

	b				
	Normal $\vec{n}_{ab}$				
a	1	2	3	4	5
1	⋯	(1,0,0)	(−0.33, 0.94, 0)	(−0.33, −0.47, 0.82)	(−0.33, −0.47, −0.82)
2	(−1, 0, 0)	⋯	(0.83,0.55,0)	(0.83, −0.28, 0.48)	(0.83, −0.28, −0.48)
3	(0.33, −0.94, 0)	(0.24,0.97,0)	⋯	(−0.54, 0.69, 0.48)	(−0.54, 0.69, −0.48)
4	(0.33, 0.47, −0.82)	(0.24, −0.48, 0.84)	(−0.54, 0.068, 0.84)	⋯	(−0.54, −0.76, 0.36)
5	(0.33,0.47,0.82)	(0.24, −0.48, −0.84)	(−0.54, 0.068, −0.84)	(−0.54, −0.76, −0.36)	⋯

TABLE III. Each cell indicates a spinor ξ_{ab} corresponding to a 3-normal of a tetrahedron.

	b				
	$\lvert\xi_{ab}\rangle$				
a	1	2	3	4	5
1	⋯	(0.71,0.71)	(0.71, −0.24 + 0.67i)	(0.95, −0.17 − 0.25i)	(0.30, −0.55 − 0.78i)
2	(0.71, −0.71)	⋯	(0.71, 0.59 + 0.39i)	(0.86, 0.48 − 0.16i)	(0.51, 0.82 − 0.27i)
3	(0.71, 0.24 − 0.67i)	(0.71, 0.17 + 0.69i)		(0.86, − 0.31 + 0.40i)	(0.51, −0.53 + 0.68i)
4	(0.30, 0.55 + 0.78i)	(0.96, 0.13 − 0.25i)	(0.96, −0.28 + 0.035i)		(0.83, −0.33 − 0.46i)
5	(0.95, 0.17 + 0.25i)	(0.28, 0.43 − 0.86i)	(0.28, −0.95 + 0.12i)	(0.57, −0.48 − 0.67i)	⋯

TABLE IV. The table of ζ_0^{ab}.

	b			
	ζ_0^{ab}			
a	2	3	4	5
1	$-3.14+0.36\gamma$	$0.68+0.36\gamma$	$5.05+0.36\gamma$	$5.05+0.36\gamma$
2	⋯	$5.05-0.59\gamma$	$-5.93-0.59\gamma$	$-3.20-0.59\gamma$
3	⋯	⋯	$-2.81-0.59\gamma$	$-5.54-0.59\gamma$
4	⋯	⋯	⋯	$-4.37-0.59\gamma$

TABLE V. Each cell of the table is the critical point of g_a.

a	1	2	3	4	5
g_{0a}	$\begin{pmatrix}1 & 0\\ 0 & 1\end{pmatrix}$	$\begin{pmatrix}0.18i & 1.01i\\ 1.01i & 0.18i\end{pmatrix}$	$\begin{pmatrix}0.18\mathrm{i} & 0.96-0.34\mathrm{i}\\ 0.96-0.34\mathrm{i} & 0.18\mathrm{i}\end{pmatrix}$	$\begin{pmatrix}1.01i & -0.48-0.34i\\ 0.48i-0.34i & -0.65i\end{pmatrix}$	$\begin{pmatrix}-0.65\mathrm{i} & -0.48-0.34\mathrm{i}\\ 0.48-0.34\mathrm{i} & 1.01\mathrm{i}\end{pmatrix}$

TABLE VI. Each cell indicates a spinor z_{ab}.

	b				
	$\lvert z_{0ab}\rangle$				
a	1	2	3	4	5
1	⋯	(1,1)	$(1,-0.333+0.942\mathrm{i})$	$(1,-0.184-0.259\mathrm{i})$	$(1,-1.817-2.569\mathrm{i})$
2	(1,1)	⋯	$(1,0.685-0.729\mathrm{i})$	$(1,1.857+0.989\mathrm{i})$	$(1,0.420+0.223\mathrm{i})$
3	$(1,0.333-0.943\mathrm{i})$	$(1,0.685-0.729\mathrm{i})$	⋯	$(1,0.313+2.080\mathrm{i})$	$(1,0.071+0.470\mathrm{i})$
4	$(1,-0.184-0.259\mathrm{i})$	$(1,1.857+0.989\mathrm{i})$	$(1,0.313+2.080\mathrm{i})$	⋯	$(1,0.058+0.082\mathrm{i})$
5	$(1,-1.817-2.569\mathrm{i})$	$(1,0.420+0.223\mathrm{i})$	$(1,0.071+0.470\mathrm{i})$	$(1,0.058+0.082\mathrm{i})$	⋯

Using (37), we shift the origin of the 54-dimensional real variables space to the saddle point s_0.

(4) The analytic continuation of the action turns all the real variables complex. We denote the analytically continued action as $\tilde{S}_{\mathrm{tot}}$ and the analytically continued g_a, $g_a^\dagger$, z_{ab}, and conjugate z_{ab} by $\bar{g}_a$, $\bar{g}'_a$, $\bar{z}_{ab}$, and $\bar{z}'_{ab}$. The s_0 is also the saddle point of $\tilde{S}_{\mathrm{tot}}$. In $\mathbb{R}^{54}$, $|\partial_\mu \tilde{S}_{\mathrm{tot}}|$ takes the minimal value 0 at s_0. Thus, we can choose the 108-ball centered at s_0 with radius 10 as the workplace of the saddle point finder. In the subspace $\mathbb{R}^{54}$, we randomly choose 200 points as the initial points of the coarse finder.

C. Results

Other than s_0, our saddle-point finder finds two more complex saddle points s_1 and s_2. At s_1, Tables XIV–XVIII show all the j_{ab}, $\bar{g}_a$, $\bar{g}'_a$, $\bar{z}_{ab}$, and $\bar{z}'_{ab}$, respectively. At s_2, Tables XIX–XXIII show all the j_{ab}, $\bar{g}_a$, $\bar{g}'_a$, $\bar{z}_{ab}$, and $\bar{z}'_{ab}$, respectively. The values of the action $\tilde{S}_{\mathrm{tot}}$ at s_0, s_1, and s_2 are $0+138.037\mathrm{i}$, $-0.334705+138.179\mathrm{i}$, and $-0.551927+137.624\mathrm{i}$. The real parts indicate that by contribution to the partition function, $s_0 > s_1 > s_2$.

D. Geometrical interpretations

The work [68] shows that the bivectors generated by group variables g_a and spinors z_{ab} and ξ_{ab} encode the geometric interpretation of a complex saddle point. Let

$$\chi'_{ab} = \frac{\mathrm{i}\gamma+\kappa_{ab}}{\mathrm{i}\gamma-1}\frac{\bar{Z}'_{ab}}{\bar{Z}'_{ab}\bar{Z}_{ab}} - \frac{\kappa_{ab}+1}{\mathrm{i}\gamma-1}\frac{\xi^\dagger_{ab}}{\xi^\dagger_{ab}\bar{Z}_{ab}},$$
$$\chi_{ab} = \frac{\mathrm{i}\gamma+\kappa_{ab}}{\mathrm{i}\gamma+1}\frac{\bar{Z}_{ab}}{\bar{Z}'_{ab}\bar{Z}_{ab}} - \frac{\kappa_{ab}-1}{\mathrm{i}\gamma+1}\frac{\xi_{ab}}{\bar{Z}'_{ab}\xi_{ab}}, \tag{53}$$

where

$$\bar{Z}'_{ab} = \bar{z}'_{ab}\bar{g}_b, \qquad \bar{Z}_{ab} = \bar{g}'_a\bar{z}_{ab},$$

and

$$k_{ab} = \begin{cases} 1, & a > b \\ -1, & a < b \end{cases}.$$

Two traceless simple bivectors of the face ab are defined by

$$B^{+}_{ab} = \chi_{ab} \otimes \bar{Z}'_{ab} - \frac{1}{2}\mathbf{1}, \tag{54}$$

$$B^{-}_{ab} = \bar{Z}_{ab} \otimes \chi'_{ab} - \frac{1}{2}\mathbf{1}. \tag{55}$$

The 4-dimensional bivectors $B_{\pm}{}^{IJ}_{ab}$ of the face ab are the spin-1 representations of $B^{\pm}_{ab}$. Namely,

$$B_{\pm}{}^{IJ}_{ab} = \begin{pmatrix} 0 & K^1_{\pm} & K^2_{\pm} & K^3_{\pm} \\ -K^1_{\pm} & 0 & J^3_{\pm} & -J^2_{\pm} \\ -K^2_{\pm} & -J^3_{\pm} & 0 & J^1_{\pm} \\ -K^3_{\pm} & J^2_{\pm} & -J^1_{\pm} & 0 \end{pmatrix},$$

where

$$K^i_{\pm} + \mathrm{i}J^i_{\pm} = \mathrm{Tr}(B^{\pm}{}_{ab}\sigma^i),$$

and σ_i are Pauli matrices. For each tetrahedron a, the closure condition reads

$$\sum_{b\in\{1\ldots5\}\backslash a} j_{ab}\kappa_{ab}B^{-}_{ab} = 0,$$
$$\sum_{b\in\{1\ldots5\}\backslash a} j_{ab}\kappa_{ab}B^{+}_{ab} = 0. \tag{56}$$

For each face ab, the parallel condition reads

$$(\bar{g}'_a)^{-1}B^{-}_{ab}\bar{g}'_a = -(\bar{g}'_b)^{-1}B^{-}_{ba}\bar{g}'_b,$$
$$\bar{g}_a B^{+}_{ab}(\bar{g}_a)^{-1} = -\bar{g}_b B^{+}_{ba}(\bar{g}_b)^{-1}. \tag{57}$$

Saddle point s_1 meets (56) and (57), while s_2 meets (56) and (57) up to an error of 10^{-5}. At either s_1 or s_2, however, for each tetrahedron a, one cannot find its four-dimensional normal N_I that meets the condition

$$\forall\, b \in \{1\ldots5\}\backslash a, \qquad B_{\pm}{}^{IJ}_{ab}N_J = \mathbf{0}.$$

Thus, both s_1 and s_2 are saddle points with Lorentzian $SO(1,3)$ bivector geometry.[5]

VI. APPLICATION: SADDLE POINTS IN THE Δ_3 EPRL SPIN FOAM MODEL

A. The action

The simplicial complex $\mathcal{K}$ considered in this section consists of three 4-simplices as in Fig. 4. We follow the convention in [21,74] to call this $\mathcal{K}$ as Δ_3. As shown in Fig. 4, we number the vertices of the Δ_3 from 1 to 6. Each 4-simplex is labeled by a single index a. We let $a = 6$ for the 4-simplex 12345, $a = 4$ for the 4-simplex 12356, and

[5]The value of $B_{\pm}$ bivectors can be found in our program.

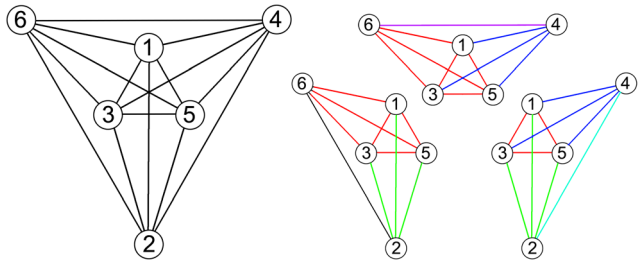

FIG. 4. The left-hand figure indicates the topological structure of the Δ_3. A Δ_3 consists six vertices and the edges connecting every two vertices. The right-hand figure shows that the Δ_3 can be decomposed into three 4-simplices.

$a = 2$ for the 4-simplex 13456. In 4-simplex a, the number pair ab labels the tetrahedron whose vertices belong to the set $\{1,\ldots,6\}\backslash\{a,b\}$. For example, five tetrahedra belonging to 4-simplex 6 are labeled by 61, 62, 63, 64, 65. The face shared by ab and ac is labeled by the triple abc. The faces in the Δ_3 are classified into three types.

(1) Type I consists the faces belonging only to a single 4-simplex. The labels of this type of the faces form the set

$$F1 = \{abc|a \in \{2,4,6\}, b,c \in \{1,3,5\}, \text{ and } b \neq c\}. \tag{58}$$

(2) Type II faces belong to the tetrahedra shared by two 4-simplices. The labels of the type II face form the set

$$F2 = \{abc|(a,b \in \{2,4,6\}, c \in \{2,4,6\}) \text{ or } \times (a,c \in \{2,4,6\}, b \in \{2,4,6\})\}. \tag{59}$$

(3) Type III faces are shared by three 4-simplices. Type III face's labels form the set

$$F3 = \{abc|a,b,c \in \{2,4,6\}\}. \tag{60}$$

The partition function of this Δ_3 spin foam is

$$Z = \sum_{\{J_{abc}|abc\in F3\}} \prod_{abc} \mathbf{d}_{J_{abc}} \int [\mathrm{d}X]\mathrm{e}^{S(X,J_{abc})}, \tag{61}$$

where

$$\begin{cases} \mathbf{d}_{J_{abc}} = 2J_{abc} + 1 \\ X \equiv (g_{ab}, z_{abc}, J^I_{abc}) \\ \mathrm{d}X \equiv (\mathrm{d}g_{ab}, \mathrm{d}\bar{z}_{abc}) \\ T \equiv (\xi_{abc}, J^B_{abc}), abc \notin F3 \end{cases}. \tag{62}$$

In (62), we denote $\{J_{abc}|abc \in F3\}$ as J^I_{abc} and $\{J_{abc}|abc \notin F3\}$ as J^B_{abc}. In contrast to (27), all the internal

ξ^I have already been integrated out and thus are not the components of X.

In our convention, the face abc is glued to the face labeled by any permutation of abc, e.g., face 624 is glued to face 642. The spinor variables z and spin variables J assigned to the glued faces fulfill the following rules.

(i) The glued faces abc and acb belong to the same 4-simplex, denoted by a, and share a spinor variable z_{abc}.
(ii) The glued faces abc and bac belong to two different 4-simplices, and each has its own spinor variable, i.e., $z_{abc} \neq z_{bac}$.
(iii) Any two glued faces share a spin variable J. Thus, for any permutation of abc, denoted as $[abc]$, $J_{abc} = J_{[abc]}$.

The X in (62) contains 15 group g variables, 30 spinor z variables, and 1 spin J variable. Each boundary face is assigned with a spinor ξ. Therefore, the T in (62) contains 36 spinor ξ parameters and 18 spin J parameters.

Note that all the spin variables are half-integer valued, and we have $\sum_{\{J_{abc}|abc\in F3\}}$ instead of $\int \mathrm{d}J_{abc}$ in (61). In order to apply our saddle-point finder, we use Poisson summation to approximate the summation over the internal spin by the integral over continuous J_{abc} in the large spin region [21]. For convenience, we introduce a scale factor λ of the spin variables, such that $J_{abc} = \lambda j_{abc}$. We apply our saddle-point finder in the case with $\lambda = 50$. In this case, the partition function is approximated by

$$Z = \int [\mathrm{d}X]\mathrm{d}\lambda j_{246} \prod_{abc} \mathbf{d}_{\lambda j_{abc}} \mathrm{e}^{\lambda S(X)}. \tag{63}$$

The action S contains three parts,

$$S = S_1 + S_2 + S_3. \tag{64}$$

Type I, Type II, and Type III faces contribute to S_1, S_2, and S_3, respectively. Let $Z_{abc} = g^{\dagger}_{ab} z_{abc}$, we have

$$S_1 = \sum_{abc\in f_1} \left(j_{abc} \ln \frac{\langle \xi_{abc}, Z_{abc}\rangle^2 \langle Z_{acb}, \xi_{acb}\rangle^2}{\langle Z_{abc}, Z_{abc}\rangle \langle Z_{acb}, Z_{acb}\rangle} + \mathrm{i}\gamma j_{abc} \ln \frac{\langle Z_{acb}, Z_{acb}\rangle}{\langle Z_{abc}, Z_{abc}\rangle} \right), \tag{65}$$

$$S_2 = \sum_{abc\in f_2} \left(j_{abc} \ln \frac{\langle \xi_{abc}, Z_{abc}\rangle^2 \langle Z_{cba}, \xi_{cba}\rangle^2}{\langle Z_{abc}, Z_{abc}\rangle \langle Z_{cba}, Z_{cba}\rangle} \times \frac{\langle Z_{acb}, Z_{cab}\rangle^2}{\langle Z_{cab}, Z_{cab}\rangle \langle Z_{acb}, Z_{acb}\rangle} + \mathrm{i}\gamma j_{abc} \ln \frac{\langle Z_{cba}, Z_{cba}\rangle}{\langle Z_{abc}, Z_{abc}\rangle} \frac{\langle Z_{acb}, Z_{acb}\rangle}{\langle Z_{cab}, Z_{cab}\rangle} \right), \tag{66}$$

and

TABLE VII. Edge lengths in 4-simplex 6.

	b				
	l_{ab}				
a	1	2	3	4	5
1	⋯	$\sqrt{11.547}$	$\sqrt{11.547}$	$\sqrt{4.272}$	$\sqrt{11.547}$
2	⋯	⋯	$\sqrt{11.547}$	$\sqrt{4.272}$	$\sqrt{11.547}$
3	⋯	⋯	⋯	$\sqrt{4.272}$	$\sqrt{11.547}$
4	⋯	⋯	⋯	⋯	$\sqrt{4.272}$

$$\begin{aligned} S_3 = {} & j_{246}\left[\ln \frac{\langle Z_{642}, Z_{462}\rangle^2}{\langle Z_{462}, Z_{462}\rangle \langle Z_{642}, Z_{642}\rangle} + \mathrm{i}\gamma \ln \frac{\langle Z_{642}, Z_{642}\rangle}{\langle Z_{462}, Z_{462}\rangle}\right] \\ & + j_{246}\left[\ln \frac{\langle Z_{426}, Z_{246}\rangle^2}{\langle Z_{246}, Z_{246}\rangle \langle Z_{426}, Z_{426}\rangle} + \mathrm{i}\gamma \ln \frac{\langle Z_{426}, Z_{426}\rangle}{\langle Z_{246}, Z_{246}\rangle}\right] \\ & + j_{246}\left[\ln \frac{\langle Z_{264}, Z_{624}\rangle^2}{\langle Z_{624}, Z_{624}\rangle \langle Z_{264}, Z_{264}\rangle} + \mathrm{i}\gamma \ln \frac{\langle Z_{264}, Z_{264}\rangle}{\langle Z_{624}, Z_{624}\rangle}\right], \end{aligned} \tag{67}$$

where

$$f_1 = \{635, 413, 453, 451, 235, 251, 231\},$$

and

$$f_2 = \{216, 416, 436, 632, 652, 654, 432, 214, 254, 615\}.$$

The γ above is the Immirzi parameter. In our work, we set $\gamma = 0.2$. We remark that the order of the numbers of each element in f_1 and f_2 and the explicit form of S_3 depend on the orientation of the Δ_3 complex.

The parameters ξ_{vef} and j^B_{abc} are given by the simplicial geometry of the Δ_3. This geometry is determined by the 15 edge lengths shown in Table VII. Here, we denote each edge by ab, with a and b the ends of the edge. Since edges 15, 35, and 13 are shared by all three 4-simplices, edges 21, 23, and 25 are shared by 4-simplices 4 and 6, and edges 41, 43, and 45 are shared by 4-simplices 2 and 6, one only needs to set the length of the edges 61, 62, 63, 62, and 64 to fix the Δ_3. In the case with cylindrical symmetry [65],

$$l_{61} = l_{63} = l_{65} = l_1, \qquad l_{62} = l_2, \qquad l_{64} = l_3.$$

We set $l_1 = \sqrt{12.8421}$, $l_2 = \sqrt{33.3319}$, and $l_3 = \sqrt{17.1054}$. The 4-normal vectors of tetrahedra 64 and 62 are

$$N_{64} = (-1, 0, 0, 0), \qquad N_{62} = (1.066, 0.369, 0, 0);$$

the 4-normal vectors of tetrahedra 46 and 42 are

$$N_{46} = (1, 0, 0, 0), \qquad N_{42} = (1, -0.00173, 0, 0);$$

the 4-normal vectors of tetrahedra 26 and 24 are

$$N_{26} = (-1.066, -0.369, 0, 0),$$
$$N_{24} = (-1.473, 1.082, 0, 0).$$

In each 4-simplex, the inner product of the 4-normal vectors of two tetrahedra defines the dihedral angle on the common face of the two tetrahedra. For example, in 4-simplex 6, the dihedral angle θ^6_{642} on face 642 satisfies

$$\cosh(\theta^6_{642}) = \eta_{ij} N^i_{64} N^j_{62}.$$

With our given edge lengths, $\theta^6_{642} = 0.361$, $\theta^4_{462} = 0.00172$, and $\theta^2_{246} = 1.2995$. The deficit angle θ^D_{246} hinged on face 246 depends on the orientation of the Δ_3 and can take one of the following 8 values

$$\theta^D_{246} = 0.3614 - 0.001726 - 1.300 = -0.9399, \quad (68)$$

$$\theta^D_{246} = 0.3614 - 0.001726 + 1.300 = 1.659, \quad (69)$$

$$\theta^D_{246} = 0.3614 + 0.001726 - 1.300 = -0.9364, \quad (70)$$

$$\theta^D_{246} = -0.3614 - 0.001726 - 1.300 = -1.662, \quad (71)$$

$$\theta^D_{246} = 0.3614 + 0.001726 + 1.300 = 1.662, \quad (72)$$

$$\theta^D_{246} = -0.3614 - 0.001726 + 1.300 = 0.9364, \quad (73)$$

$$\theta^D_{246} = -0.3614 + 0.001726 - 1.300 = -1.659, \quad (74)$$

$$\theta^D_{246} = -0.3614 + 0.001726 + 1.300 = 0.9399. \quad (75)$$

With these edge lengths, one can compute the 3-normal vector of each face in Δ_3, and use these 3-normal vectors to build the ξ and the j^B. Tables VIII–X record the values of ξ.

TABLE VIII. Values of ξ_{6ab}.

	b				
	ξ_{6ab}				
a	1	2	3	4	5
1	⋯	(0.2887, −0.9534 + 0.0878i)	(0.9574, −0.1667 − 0.2357i)	(1,0)	(0.9574, −0.1208 + 0.2622i)
2	(0.9574, −0.25 − 0.1443i)	⋯	(0.2887, −0.8292 + 0.4787i)	(0,1)	(0.2887, −0.9574i)
3	(0.2887, −0.5528 − 0.7817i)	(0.9574, 0.1208 − 0.2622i)	⋯	(1,0)	(0.9574, −0.2875 + 0.02649i)
4	(0.9530, 0.1749 + 0.2473i)	(0.7071,0.7071)	(0.3029, 0.5502 + 0.7781i)	⋯	(0.7071, −0.2357 + 0.6667i)
5	(0.2887, 0.1750 + 0.9413i)	(0.9574, 0.2722 + 0.09623i)	(0.2887, 0.7277 − 0.6222i)	(0, 0.9701 + 0.2425i)	⋯

TABLE IX. Values of ξ_{4ab}.

	b				
	ξ_{4ab}				
a	1	2	3	5	6
1	⋯	(0.9467, 0.1348 − 0.2926i)	(0.9530, −0.1749 − 0.2473i)	(0.3029, −0.9490 + 0.08744i)	(0, −0.6247 − 0.7809i)
2	(0.8096, 0.5083 − 0.2935i)	⋯	(0.5870, 0.7011 + 0.4048i)	(0.8096, 0.5870i)	(1,0)
3	(0.3029, −0.5502 − 0.7781i)	(0.3221, −0.9427 + 0.08686i)	⋯	(0.3029, −0.3988 + 0.8656i)	(0, 0.5145 + 0.8575i)
5	(0.9530, 0.2302 − 0.1968i)	(0.9467, 0.3037 + 0.1074i)	(0.9530, 0.05535 + 0.2978i)	⋯	(1,0)
6	(0.9530, 0.1749 + 0.2473i)	(0.7071,0.7071)	(0.3029, 0.5502 + 0.7781i)	(0.7071, −0.2357 + 0.6667i)	⋯

TABLE X. Values of ξ_{2ab}.

	b				
	ξ_{2ab}				
a	1	3	4	5	6
1	⋯	(0.9685, −0.2171 − 0.1220i)	(0.9590, −0.09545 − 0.2667i)	(0.9685, 0.09038 − 0.2320i)	(0.9985, 0.01820 + 0.05084i)
3	(0.2490, −0.8443 − 0.4745i)	⋯	(0.2833, −0.9393 + 0.1935i)	(0.2490, −0.5880 + 0.7696i)	(0.05400, 0.9780 − 0.2015i)
4	(0.8096, 0.5083 − 0.2935i)	(0.5870, 0.7011 + 0.4048i)	⋯	(0.8096, 0.5870i)	(1,0)
5	(0.2490, −0.9684 − 0.01161i)	(0.9685, 0.03190 + 0.2469i)	(0.9590, 0.2116 + 0.1883i)	⋯	(0.05400, 0.7460 + 0.6638i)
6	(0.9574, −0.25 − 0.1443i)	(0.2887, −0.8292 + 0.4787i)	(0,1)	(0.2887, −0.9574i)	⋯

TABLE XI. The j^b_{6ab}.

	b				
	j^b_{6ab}				
a	1	2	3	4	5
1	⋯	2	2	5	2
2	2	⋯	2	⋯	2
3	2	2	⋯	5	2
4	5	⋯	5	⋯	5
5	2	2	2	5	⋯

TABLE XII. The j^b_{4ab}.

	b				
	j^b_{4ab}				
a	1	2	3	5	6
1	⋯	5.361	5.663	5.663	5
2	5.361	⋯	5.361	5.361	⋯
3	5.663	5.361	⋯	5.663	5
5	5.663	5.361	5.663	⋯	5
6	5	⋯	5	5	⋯

TABLE XIII. The j^b_{2ab}.

	b				
	j^b_{2ab}				
a	1	3	4	5	6
1	⋯	3.704	5.361	3.704	2
3	3.704	⋯	5.361	3.704	2
4	5.361	5.361	⋯	5.361	⋯
5	3.704	3.704	5.361	⋯	2
6	2	2	⋯	2	⋯

Tables XI–XIII record the variables j^B. Many values in Tables XII and XIII are not half-integers; however, at large λ, the difference between λj^B and its closest half integer is negligible. Therefore, a λj^B can be approximately regarded as a half-integer spin variable.

B. Pretreatments

We have the following pretreatments:

(1) We fix the gauges (32) and (33) by parametrizing the group variables as follows. The $\mathrm{SL}(2,\mathbb{C})$ gauge on each 4-simplex is fixed by restricting g_{61}, g_{45}, and g_{23} to be the identity matrix. The SU(2) gauge on each internal tetrahedron is fixed by parametrizing g_{64}, g_{42}, and g_{26} as in (35). The group variables $g_{65}, g_{63}, g_{43}, g_{41}, g_{25}, g_{21}, g_{62}, g_{46}, g_{24}$ are parametrized as in (36)

(2) All the z variables are parametrized as (34). All the js are already real variables and hence needs no additional parametrization.

(3) The works [63,64,70,75–80] pointed out that the simplicial geometry defines the critical points of the spin foam action $X_a = (j_a, z_a, g_a)$, such that

$$\mathrm{Re}(S(X_a)) = 0,$$
$$\partial_g S|_{X_a} = 0,$$
$$\partial_z S|_{X_a} = 0.$$

In our case with curvature, these critical points are not saddle points because

$$\mathrm{Im}(\partial_{j_{246}} S|_{X_a}) = \gamma\lambda\theta^D_{246}.$$

Such critical points and the points close to them can still be the initial points of our saddle-point finder.

Corresponding to the simplicial geometry with deficit angle (68), the g^0_{ab} and z^0_{abc} of a critical point X_0 are given in Tables XXIV–XXVII, and j^0_{246} is 5. We shift the origin of the space of our real variables to X_0 by plugging g^0_{ab} and z^0_{abc} into (37). In this parametrization, the action S depends on 124 real variables.

Seven more critical points can be found by acting parity flip operation on X_0. On each 4-simplex, the parity flip is a transformation between two critical points $(g^0_{ab}, z^0_{abc}, j^0_{abc})$ and $(\tilde{g}^0_{ab}, \tilde{z}^0_{abc}, \tilde{j}^0_{abc})$, where

$$\tilde{g}^0_{ab} = (g^{0\dagger}_{ab})^{-1},$$

$$\tilde{z}^0_{abc} = \frac{g^0_{ab} g^{0\dagger}_{ab} z^0_{abc}}{||g^{0\dagger}_{ab} z^0_{abc}||^2},$$

and

$$\tilde{j}^0_{abc} = j^0_{abc}.$$

In Δ_3, including the identity, there are 2^3 different ways of parity flipping. Acting these flippings on X_0 results in 7 more critical points. These critical points corresponding to the simplicial geometries with deficit angles (69) to (75). Using the technique introduced in Appendix C, one can find the coordinates of those critical points in our parametrization.

(4) Similar to the single 4-simplex case, the analytic continuation of the action changes all the real variables into complex. We denote the analytically continued action as $\tilde{S}$ and the analytically continued g_{ab}, $g^\dagger_{ab}$, z_{abc}, and conjugate z_{abc} as $\bar{g}_{ab}$, $\bar{g}'_{ab}$, $\bar{z}_{abc}$, and $\bar{z}'_{abc}$. The j_{246} is analytically continued as $\tilde{j}_{246}$.

The distances between the seven additional critical points and X_0 are smaller than 21. Therefore, we choose the 248-ball centered at X_0 with radius 21 as the workplace of the saddle point finder. In the subspace $\mathbb{R}^{124}$, we randomly choose 1600 points closing to the critical points, and feed them to our saddle-point finder.

C. Results

The saddle-point finder finds 112 points. The $\partial_\mu \tilde{S}$ at all these points are smaller than 10^{-11}, so we can safely consider all 112 points as the saddle points of the $\tilde{S}$. We store the exact values of the $(\tilde{S}, \bar{g}_{ab}, \bar{g}'_{ab}, \bar{z}_{abc}, \bar{z}'_{abc}, \tilde{j}_{246})$ at each saddle points in [81]. We can compute the real part of $\tilde{S}$. In our computation, we find 44 saddle points have positive real part of the action. By [30], we know that the saddle points attached to the Lefschetz thimbles have negative real part of the action. Hence, those 44 saddle points with positive real part of the action are attached with the antithimbles and do not contribute to the partition function. The other 68 saddle points with negative real part of the action contribute to the partition function, and each point's contribution can be estimated by its real part of the action.

D. Geometrical interpretations

As we mentioned, the geometrical interpretation of the saddle points is encoded in the bivectors. For each face abc, two bivectors can be defined

$$B^{+}_{abc} = \chi_{abc} \otimes \bar{Z}'_{abc} - \frac{1}{2}\mathbf{1}, \tag{76}$$

$$B^{-}_{abc} = \bar{Z}_{abc} \otimes \chi'_{abc} - \frac{1}{2}\mathbf{1}. \tag{77}$$

When $b \in \{1,3,5\}$, the face abc is a boundary face, and its χ'_{abc} and χ_{abc} read

$$\begin{aligned}\chi'_{abc} &= \frac{i\gamma+\kappa_{abc}}{i\gamma-1}\frac{\bar{Z}'_{abc}}{\bar{Z}'_{abc}\bar{Z}_{abc}} - \frac{\kappa_{abc}+1}{i\gamma-1}\frac{\xi^{\dagger}_{abc}}{\xi^{\dagger}_{abc}\bar{Z}_{abc}},\\ \chi_{abc} &= \frac{i\gamma+\kappa_{abc}}{i\gamma+1}\frac{\bar{Z}_{abc}}{\bar{Z}'_{abc}\bar{Z}_{abc}} - \frac{\kappa_{abc}-1}{i\gamma+1}\frac{\xi_{abc}}{\bar{Z}'_{abc}\xi_{abc}}.\end{aligned} \tag{78}$$

When $b \in \{2,4,6\}$, the face abc is a bulk face, and

$$\begin{aligned}\chi'_{abc} &= \frac{i\gamma+\kappa_{abc}}{i\gamma-1}\frac{\bar{Z}'_{abc}}{\bar{Z}'_{abc}\bar{Z}_{abc}} - \frac{\kappa_{abc}+1}{i\gamma-1}\frac{\bar{Z}'_{abc}}{\bar{Z}'_{abc}\bar{Z}_{abc}},\\ \chi_{abc} &= \frac{i\gamma+\kappa_{abc}}{i\gamma+1}\frac{\bar{Z}_{abc}}{\bar{Z}'_{abc}\bar{Z}_{abc}} - \frac{\kappa_{abc}-1}{i\gamma+1}\frac{\bar{Z}_{abc}}{\bar{Z}'_{abc}\bar{Z}_{abc}}.\end{aligned} \tag{79}$$

The κ_{abc} depends the orientation of the Δ_3. Namely, $\kappa_{abc} = -1$ for the faces 612, 614, 623, 625, 631, 634, 651, 653, 412, 415, 423, 426, 431, 435, 451, 456, 461, 463, 213, 215, 234, 236, 241, 245, 253, 256, 361, and 264, otherwise $\kappa_{abc} = 1$. For each tetrahedron ab, the closure condition is given by

$$\begin{aligned}\sum_{c\in\{1\ldots6\}\setminus\{ab\}} j_{abc}\kappa_{abc}B^{-}_{abc} = 0,\\ \sum_{c\in\{1\ldots6\}\setminus\{ab\}} j_{abc}\kappa_{abc}B^{+}_{abc} = 0.\end{aligned} \tag{80}$$

For each face abc, the parallel condition reads

$$\begin{aligned}(\bar{g}'_{ab})^{-1}B^{-}_{abc}\bar{g}'_{ab} &= -(\bar{g}'_{ac})^{-1}B^{-}_{acb}\bar{g}'_{ac}, \qquad \bar{g}_{ab}B^{+}_{abc}(\bar{g}_{ab})^{-1}\\ &= -\bar{g}_{ac}B^{+}_{acb}(\bar{g}_{ac})^{-1}.\end{aligned} \tag{81}$$

All the saddle points satisfy the closure condition and the parallel condition; however, the four-dimensional normal vectors of the tetrahedra in the Δ_3 do not exist. Therefore, these saddle points give rise to Lorentzian $SO(1,3)$ bivector geometry.

VII. CONCLUSION

We have developed our saddle-point finder to find the complex saddle points for any given action. Applying the saddle-point finder to two examples in the spin foam model, we find the complex saddle points and estimate their contributions to the partition function. Finding these saddle points would help not only the asymptotic analysis of the analytically continued spin foam model but also the Lefschetz thimble Monte Carlo computation in the regime of small j, because in this regime, the nonperturbative contribution due to the complex saddle points is non-negligible.

In the example of the Δ_3 spin foam model, all of the saddle points we have found do not correspond to simplicial geometry. This result enforced the conclusion in [21,55], i.e., the classical limit of the spin foam model should be taken in the limit with large-j but small deficit angles. Yet, the explicit relation between the complex saddle points and real saddle points [21] is not clear. In future works we shall also explore how the complex critical points would influence the renormalization procedure of the spin foam model and the exact meaning of the complex critical points in the semiclassical limit. Our saddle-point finder is one of the essential tools for those further researches. For example, one can deform the boundary state in the Δ_3 spin foam model from the flat geometry boundary to the curved geometry boundary, and use the saddle-point finder to explore how the real saddle points can evolve into complex saddle points with respect to the deformation of the boundary state; one can also apply the saddle-point finder in the Pachner move scheme of the spin foam to see how the number of the complex saddle points would change with different discretization schemes.

In this paper, we use the information of the simplicial geometry to help us to narrow down the region to find the complex saddle points. In future works, instead of using the physical information, we would like to employ certain optimization algorithm in the pretreatment stage to automatically find the proper region to be the workplace for our finder. This optimization will improve our saddle-point finder to be a "black-box" that is applicable to other physical system other than loop quantum gravity.

ACKNOWLEDGMENTS

Y. W. is supported by NSFC Grant No. 11875109, General Program of Science and Technology of Shanghai No. 21ZR1406700, and Shanghai Municipal Science and Technology Major Project (Grant No. 2019SHZDZX01). Y. W. is also grateful to the Perimeter Institute for Theoretical Physics for hospitality during his visit, where the work is finalized. Z. H. thanks Hongguang Liu for the useful discussions.

APPENDIX A: SADDLE POINTS OF SINGLE 4-SIMPLEX SPIN FOAM MODEL

TABLE XIV. The values of j_{ab} at s_1.

	b			
	j_{ab}			
a	2	3	4	5
1	$4.947 + 3.013 \times 10^{-4}\mathrm{i}$	$4.946 + 2.766 \times 10^{-4}\mathrm{i}$	$4.948 + 3.358 \times 10^{-4}\mathrm{i}$	$4.951 + 4.880 \times 10^{-4}\mathrm{i}$
2	⋯	$2.018 + 1.267 \times 10^{-3}\mathrm{i}$	$2.019 + 1.383 \times 10^{-3}\mathrm{i}$	$2.021 + 1.490 \times 10^{-3}\mathrm{i}$
3	⋯	⋯	$2.019 + 1.341 \times 10^{-3}\mathrm{i}$	$2.021 + 1.448 \times 10^{-3}\mathrm{i}$
4	⋯	⋯	⋯	$2.0198 + 1.386 \times 10^{-3}\mathrm{i}$

TABLE XV. The values of g_a at s_1.

a	g_a
1	$\begin{pmatrix} 1 & 0 \\ 0 & 1 \end{pmatrix}$
2	$\begin{pmatrix} 1.793 \times 10^{-2} + (4.688 \times 10^{-4})\mathrm{i} & 1.793 \times 10^{-2} + (4.688 \times 10^{-4})\mathrm{i} \\ -5.331 \times 10^{-5} + 1\mathrm{i} & 1.832 \times 10^{-2} + (4.071 \times 10^{-4})\mathrm{i} \end{pmatrix}$
3	$\begin{pmatrix} 1.827 \times 10^{-2} + (6.071 \times 10^{-4})\mathrm{i} & 9.425 \times 10^{-1} - (3.332 \times 10^{-1})\mathrm{i} \\ -9.428 \times 10^{-1} - (3.333 \times 10^{-1})\mathrm{i} & 1.797 \times 10^{-2} + (4.961 \times 10^{-4})\mathrm{i} \end{pmatrix}$
4	$\begin{pmatrix} 1.814 \times 10^{-2} + (8.171 \times 10^{-1})\mathrm{i} & -4.712 \times 10^{-1} - (3.332 \times 10^{-1})\mathrm{i} \\ 4.714 \times 10^{-1} - (3.333 \times 10^{-1})\mathrm{i} & 1.809 \times 10^{-2} - (8.158 \times 10^{-1})\mathrm{i} \end{pmatrix}$
5	$\begin{pmatrix} 1.811 \times 10^{-2} - (8.156 \times 10^{-1})\mathrm{i} & -4.713 \times 10^{-1} - (3.333 \times 10^{-1})\mathrm{i} \\ 4.713 \times 10^{-1} - (3.332 \times 10^{-1})\mathrm{i} & 1.81 \times 10^{-2} + (8.171 \times 10^{-1})\mathrm{i} \end{pmatrix}$

TABLE XVI. The values of $g_a^\dagger$ at s_1.

a	$g_a^\dagger$
1	$\begin{pmatrix} 1 & 0 \\ 0 & 1 \end{pmatrix}$
2	$\begin{pmatrix} 1.832 \times 10^{-2} + (4.071 \times 10^{-4})\mathrm{i} & -6.919 \times 10^{-5} - (9.997 \times 10^{-1})\mathrm{i} \\ 5.331 \times 10^{-5} - 1\mathrm{i} & 1.793 \times 10^{-2} + (4.688 \times 10^{-4})\mathrm{i} \end{pmatrix}$
3	$\begin{pmatrix} 1.797 \times 10^{-2} + (4.961 \times 10^{-4})\mathrm{i} & -9.425 \times 10^{-1} + (3.332 \times 10^{-1})\mathrm{i} \\ 9.428 \times 10^{-1} + (3.333 \times 10^{-1})\mathrm{i} & 1.827 \times 10^{-2} + (6.071 \times 10^{-4})\mathrm{i} \end{pmatrix}$
4	$\begin{pmatrix} 1.809 \times 10^{-2} - (8.158 \times 10^{-1})\mathrm{i} & 4.712 \times 10^{-1} + (3.332 \times 10^{-1})\mathrm{i} \\ -4.714 \times 10^{-1} + (3.333 \times 10^{-1})\mathrm{i} & 1.814 \times 10^{-2} + (8.171 \times 10^{-1})\mathrm{i} \end{pmatrix}$
5	$\begin{pmatrix} 1.81 \times 10^{-2} + (8.171 \times 10^{-1})\mathrm{i} & 4.713 \times 10^{-1} + (3.332 \times 10^{-1})\mathrm{i} \\ -4.713 \times 10^{-1} + (3.333 \times 10^{-1})\mathrm{i} & 1.811 \times 10^{-2} - (8.156 \times 10^{-1})\mathrm{i} \end{pmatrix}$

TABLE XVII. Values of z_{ab} at s_1.

	b				
	$\|z_{ab}\rangle$				
a	1	2	3	4	5
1	⋯	(1,1)	$(1, -0.3333 + 0.9428\mathrm{i})$	$(1, -0.1835 - 0.2595\mathrm{i})$	$(1, -1.816 - 2.569\mathrm{i})$
2	(1,1)	⋯	$(1, 0.8507 - 0.5636\mathrm{i})$	$(1, 1.568 + 0.5511\mathrm{i})$	$(1, 0.5603 + 0.1737\mathrm{i})$
3	$(1, -0.3333 + 0.9428\mathrm{i})$	$(1, 0.8507 - 0.5636\mathrm{i})$	⋯	$(1, -0.067 + 1.704\mathrm{i})$	$(1, -0.001082 + 0.6021\mathrm{i})$
4	$(1, -0.1835 - 0.2595\mathrm{i})$	$(1, 1.568 + 0.5511\mathrm{i})$	$(1, -0.067 + 1.704\mathrm{i})$	⋯	$(1, -0.01705 - 0.006849\mathrm{i})$
5	$(1, -1.816 - 2.569\mathrm{i})$	$(1, 0.5603 + 0.1737\mathrm{i})$	$(1, -0.001082 + 0.6021\mathrm{i})$	$(1, -0.01705 - 0.006849\mathrm{i})$	⋯

TABLE XVIII. Values of conjugate z_{ab} at s_1.

	b				
	$\langle z_{ab}\|$				
a	1	2	3	4	5
1	⋯	$(1, 0.9997 - 0.0005081\mathrm{i})$	$(1, -0.3328 - 0.9426\mathrm{i})$	$(1, -0.1834 + 0.2593\mathrm{i})$	$(1, -1.817 + 2.569\mathrm{i})$
2	$(1, 0.9997 - 0.0005081\mathrm{i})$	⋯	$(1, 0.8145 + 0.6141\mathrm{i})$	$(1, 1.633 - 0.6519\mathrm{i})$	$(1, 0.5211 - 0.1853\mathrm{i})$
3	$(1, -0.3328 - 0.9426\mathrm{i})$	$(1, 0.8145 + 0.6141\mathrm{i})$	⋯	$(1, 0.003138 - 1.808\mathrm{i})$	$(1, 0.02253 - 0.568\mathrm{i})$
4	$(1, -0.1834 + 0.2593\mathrm{i})$	$(1, 1.633 - 0.6519\mathrm{i})$	$(1, 0.003138 - 1.808\mathrm{i})$	⋯	$(1, 0.0007018 - 0.01837\mathrm{i})$
5	$(1, -1.817 + 2.569\mathrm{i})$	$(1, 0.5211 - 0.1853\mathrm{i})$	$(1, 0.02253 - 0.568\mathrm{i})$	$(1, 0.0007018 - 0.01837\mathrm{i})$	⋯

TABLE XIX. The values of j_{ab} at s_2.

	b			
	j_{ab}			
a	2	3	4	5
1	$4.976 - 0.07024\mathrm{i}$	$4.976 - 0.07097\mathrm{i}$	$4.977 - 0.06961\mathrm{i}$	$4.977 - 0.06565\mathrm{i}$
2	⋯	$2.004 + 0.02366\mathrm{i}$	$2.004 + 0.02595\mathrm{i}$	$2.005 + 0.0285\mathrm{i}$
3	⋯	⋯	$2.004 + 0.02514\mathrm{i}$	$2.005 + 0.0277\mathrm{i}$
4	⋯	⋯	⋯	$2.005 + 0.02678\mathrm{i}$

TABLE XX. The values of g_a at s_2.

a	g_a
1	$\begin{pmatrix} 1 & 0 \\ 0 & 1 \end{pmatrix}$
2	$\begin{pmatrix} -8.793 \times 10^{-2} - (1.918 \times 10^{-1})\mathrm{i} & 1.683 \times 10^{-2} + 1.015\mathrm{i} \\ 1.632 \times 10^{-2} + 1.014\mathrm{i} & -8.766 \times 10^{-2} - (1.913 \times 10^{-1})\mathrm{i} \end{pmatrix}$
3	$\begin{pmatrix} -8.788 \times 10^{-2} - (1.913 \times 10^{-1})\mathrm{i} & 9.508 \times 10^{-1} - (3.539 \times 10^{-1})\mathrm{i} \\ -9.621 \times 10^{-1} - (3.228 \times 10^{-1})\mathrm{i} & -8.785 \times 10^{-2} - (1.918 \times 10^{-1})\mathrm{i} \end{pmatrix}$
4	$\begin{pmatrix} -7.448 \times 10^{-2} + (6.368 \times 10^{-1})\mathrm{i} & -4.838 \times 10^{-1} - (3.3 \times 10^{-1})\mathrm{i} \\ 4.728 \times 10^{-1} - (3.459 \times 10^{-1})\mathrm{i} & -1.015 \times 10^{-1} - 1.02\mathrm{i} \end{pmatrix}$
5	$\begin{pmatrix} -1.018 \times 10^{-1} - 1.02\mathrm{i} & -4.838 \times 10^{-1} - (3.303 \times 10^{-1})\mathrm{i} \\ 4.727 \times 10^{-1} - (3.46 \times 10^{-1})\mathrm{i} & -7.463 \times 10^{-2} + (6.368 \times 10^{-1})\mathrm{i} \end{pmatrix}$

TABLE XXI. The values of $g_a^\dagger$ at s_2.

a	$g_a^\dagger$
1	$\begin{pmatrix} 1 & 0 \\ 0 & 1 \end{pmatrix}$
2	$\begin{pmatrix} 1.588\times10^{-1}+(1.664\times10^{-1})\mathrm{i} & -2.647\times10^{-2}-1.002\mathrm{i} \\ -2.619\times10^{-2}-1.002\mathrm{i} & 1.586\times10^{-1}+(1.659\times10^{-1})\mathrm{i} \end{pmatrix}$
3	$\begin{pmatrix} 1.585\times10^{-1}+(1.661\times10^{-1})\mathrm{i} & -9.354\times10^{-1}+(3.588\times10^{-1})\mathrm{i} \\ 9.531\times10^{-1}+(3.092\times10^{-1})\mathrm{i} & 1.585\times10^{-1}+(1.665\times10^{-1})\mathrm{i} \end{pmatrix}$
4	$\begin{pmatrix} 1.37\times10^{-1}-(6.516\times10^{-1})\mathrm{i} & 4.81\times10^{-1}+(3.213\times10^{-1})\mathrm{i} \\ -4.634\times10^{-1}+(3.462\times10^{-1})\mathrm{i} & 1.798\times10^{-1}+(9.842\times10^{-1})\mathrm{i} \end{pmatrix}$
5	$\begin{pmatrix} 1.798\times10^{-1}+(9.84\times10^{-1})\mathrm{i} & 4.81\times10^{-1}+(3.214\times10^{-1})i \\ -4.635\times10^{-1}+(3.463\times10^{-1})\mathrm{i} & 1.369\times10^{-1}-(6.516\times10^{-1})\mathrm{i} \end{pmatrix}$

TABLE XXII. Values of z_{ab} at s_2.

	b				
	$\lvert z_{ab}\rangle$				
a	1	2	3	4	5
1	⋯	$(1, 1-0.00007656\mathrm{i})$	$(1, -0.3334+0.9427\mathrm{i})$	$(1, -0.1835-0.2595\mathrm{i})$	$(1, -1.816-2.569\mathrm{i})$
2	$(1, 1-0.00007656\mathrm{i})$	⋯	$(1, 1.044-0.4492\mathrm{i})$	$(1, 1.258+0.4235\mathrm{i})$	$(1, 0.6495+0.06107\mathrm{i})$
3	$(1, 1.044-0.4492\mathrm{i})$	$(1, 0.8507-0.5636\mathrm{i})$	⋯	$(1, -0.3736+1.486\mathrm{i})$	$(1, -0.01186+0.753\mathrm{i})$
4	$(1, 1.258+0.4235\mathrm{i})$	$(1, 1.568+0.5511\mathrm{i})$	$(1, -0.3736+1.486\mathrm{i})$	⋯	$(1, -0.113-0.04805\mathrm{i})$
5	$(1, -1.816-2.569\mathrm{i})$	$(1, 0.6495+0.06107\mathrm{i})$	$(1, -0.01186+0.753\mathrm{i})$	$(1, -0.113-0.04805\mathrm{i})$	⋯

TABLE XXIII. Values of conjugate z_{ab} at s_2.

	b				
	$\langle z_{ab}\rvert$				
a	1	2	3	4	5
1	⋯	$(1, 1.001-0.0006011\mathrm{i})$	$(1, -0.3335-0.9421\mathrm{i})$	$(1, -0.1832+0.2596\mathrm{i})$	$(1, -1.816+2.569\mathrm{i})$
2	$(1, 1.001-0.0006011\mathrm{i})$	⋯	$(1, 0.8086+0.3475\mathrm{i})$	$(1, 1.527-0.1443\mathrm{i})$	$(1, 0.7141-0.2405\mathrm{i})$
3	$(1, -0.3335-0.9421\mathrm{i})$	$(1, 0.8086+0.3475\mathrm{i})$	⋯	$(1, -0.0209-1.327\mathrm{i})$	$(1, -0.1588-0.6324\mathrm{i})$
4	$(1, -0.1832+0.2596\mathrm{i})$	$(1, 1.527-0.1443\mathrm{i})$	$(1, -0.0209-1.327\mathrm{i})$	⋯	$(1, -0.007496+0.1226\mathrm{i})$
5	$(1, -1.816+2.569\mathrm{i})$	$(1, 0.7141-0.2405\mathrm{i})$	$(1, -0.1588-0.6324\mathrm{i})$	$(1, -0.007496+0.1226\mathrm{i})$	⋯

APPENDIX B: THE SADDLE POINT X_0

TABLE XXIV. The table of g^0_{ab}.

	a		
	g^0_{ab}		
b	6	4	2
1	$\begin{pmatrix} 0.9553 & -0.2955i \\ -0.2955i & 0.9553 \end{pmatrix}$	$\begin{pmatrix} -0.3900+0.6198i & -0.1417-0.6688i \\ 0.1401-0.6650i & -0.3888-0.6193i \end{pmatrix}$	$\begin{pmatrix} 0.7052+0.04132i & -0.1336-0.3004i \\ 2.173-1.447i & 0.3506-0.6723i \end{pmatrix}$
2	$\begin{pmatrix} 0.4515+0.5054i & -1.042-0.4024i \\ 0.4792-0.2790i & 0.4896-0.3313i \end{pmatrix}$	$\begin{pmatrix} 0.1784-0.6465i & 0.4982-0.5489i \\ -0.4970-0.5489i & 0.1799+0.6483i \end{pmatrix}$	⋯
3	$\begin{pmatrix} 0.8343-0.1999i & 0.6464+0.7435i \\ -0.3138+0.2731i & 0.6888+0.09706i \end{pmatrix}$	$\begin{pmatrix} 0.2856+0.1372i & 0.1484-0.9387i \\ -0.1479-0.9346i & 0.2869-0.1373i \end{pmatrix}$	$\begin{pmatrix} 0.9553 & -0.2955i \\ -0.2955i & 0.9553 \end{pmatrix}$
4	$\begin{pmatrix} 0.6724+0.06192i & -0.2002-0.5181i \\ 0.1395-0.5346i & 1.030-0.04314i \end{pmatrix}$	⋯	$\begin{pmatrix} 1.2080+0.2345i & 0.8229-0.2524i \\ -1.094+0.1394i & 0.1679+0.2911i \end{pmatrix}$
5	$\begin{pmatrix} 0.1820-0.2099i & 0.08676-1.274i \\ -0.01552-0.7019i & 0.3588+0.1879i \end{pmatrix}$	$\begin{pmatrix} 0.9553 & -0.2955i \\ -0.2955i & 0.9553 \end{pmatrix}$	$\begin{pmatrix} 0.7194-0.2650i & -0.1255-0.06036i \\ 0.7314+2.2003i & 1.419+0.07753i \end{pmatrix}$
6	⋯	$\begin{pmatrix} 0.4773-0.06975i & 0.2255-0.8464i \\ -0.2249-0.8453i & 0.4797+0.06956i \end{pmatrix}$	$\begin{pmatrix} 2.096-0.2671i & -0.3216-0.5575i \\ 0.6308+0.1225i & 0.4297-0.1318i \end{pmatrix}$

TABLE XXV. The table of z^0_{6ab}.

	b				
	z^0_{6ab}				
a	1	2	3	4	5
1	⋯	$(1,-1.615+1.503i)$	$(1,-0.2227-0.5883i)$	$(1,-0.3093i)$	$(1,-0.1173-0.02850i)$
2	$(1,-1.615+1.503i)$	⋯	$(1,0.5763-0.03732i)$	$(1,0.5401-0.2764i)$	$(1,0.7037-0.4995i)$
3	$(1,-0.2227-0.5883i)$	$(1,0.5763-0.03732i)$	⋯	$(1,0.3919+0.4517i)$	$(1,-0.03505+0.2601i)$
4	$(1,-0.3093i)$	$(1,0.5401-0.2764i)$	$(1,0.3919+0.4517i)$	⋯	$(1,-0.1737+0.1311i)$
5	$(1,-0.1173-0.02850i)$	$(1,0.7037-0.4995i)$	$(1,-0.03505+0.2601i)$	$(1,-0.1737+0.1311i)$	⋯

TABLE XXVI. The table of z^0_{4ab}.

	b				
	z^0_{4ab}				
a	1	2	3	5	6
1	⋯	$(1,-0.1445+0.9792i)$	$(1,-0.2163+0.5057i)$	$(1,0.3001-0.5271i)$	$(1,0.7687-0.7459i)$
2	$(1,-0.1445+0.9792i)$	⋯	$(1,-0.2137+0.1556i)$	$(1,0.3251-0.1581i)$	$(1,0.9837+0.4936i)$
3	$(1,-0.2163+0.5057i)$	$(1,-0.2137+0.1556i)$	⋯	$(1,0.05290+0.003738i)$	$(1,0.09562+0.3193i)$
5	$(1,0.3001-0.5271i)$	$(1,0.3251-0.1581i)$	$(1,0.05290+0.003738i)$	⋯	$(1,-0.3093i)$
6	$(1,0.7687-0.7459i)$	$(1,0.9837+0.4936i)$	$(1,0.09562+0.3193i)$	$(1,-0.3093i)$	⋯

TABLE XXVII. The table of z^0_{2ab}.

	b				
	z^0_{2ab}				
a	1	3	4	5	6
1	⋯	$(1, -2.928 + 2.087\mathrm{i})$	$(1, -3.280 + 2.139\mathrm{i})$	$(1, -3.498 + 1.795\mathrm{i})$	$(1, -2.962 + 1.585\mathrm{i})$
3	$(1, -2.928 + 2.087\mathrm{i})$	⋯	$(1, -1.442 + 1.530\mathrm{i})$	$(1, -0.5935 + 1.644\mathrm{i})$	$(1, 0.6318 + 3.250\mathrm{i})$
4	$(1, -3.280 + 2.139\mathrm{i})$	$(1, -1.442 + 1.530\mathrm{i})$	⋯	$(1, -0.5022 + 1.623\mathrm{i})$	$(1, 1.268 + 3.028\mathrm{i})$
5	$(1, -3.498 + 1.795\mathrm{i})$	$(1, -0.5935 + 1.644\mathrm{i})$	$(1, -0.5022 + 1.623\mathrm{i})$	⋯	$(1, 2.085 + 3.439\mathrm{i})$
6	$(1, -2.962 + 1.585\mathrm{i})$	$(1, 0.6318 + 3.250\mathrm{i})$	$(1, 1.268 + 3.028\mathrm{i})$	$(1, 2.085 + 3.439)$	⋯

APPENDIX C: PARITY FLIPPING

In Sec. VI, g_{64}, g_{42}, and g_{26} are parametrized as in (35). Considering a parity flip at 4-simplex 6, the saddle point values of g_{64} and g_{46} are $(g^{0\dagger}_{64})^{-1}$ and g^0_{46}. In fact, there is no upper triangular matrix T, such that $g^0_{64}T = (g^{0\dagger}_{64})^{-1}$. But the parametrization used in Sec. VI is still compatible with the parity flipping. By SU(2) gauge, $g_{64} = (g^{0\dagger}_{64})^{-1}$, $g_{46} = g^0_{46}$ is equivalent to $g_{64} = (g^{0\dagger}_{64})^{-1}U$, $g_{46} = g^0_{46}U$, where $U \in \mathrm{SU}(2)$. One can always find a upper triangular matrix T such that $g^0_{64}T = (g^{0\dagger}_{64})^{-1}U$. Thus, the parity flipped saddle point with $g_{64} = (g^{0\dagger}_{64})^{-1}U$, $g_{46} = g^0_{46}U$ can be expressed in our parametrization. Explicitly, solving the equation

$$(g^{0\dagger}_{64}g^0_{64})^{-1} \cdot ((g^{0\dagger}_{64}g^0_{64})^{-1})^\dagger = T \cdot T^\dagger$$

results in T, and

$$U = g^{0\dagger}_{64}g^0_{64}T.$$

The parity flip on 4-simplex 4 or on 4-simplex 2 can be treated similarly.

APPENDIX D: GELMAN-RUBIN DIAGNOSTIC

Gelman-Rubin diagnostic (GRD) [82–84] is a general approach to monitor the convergence of the Markov chain Monte Carlo. GRD tests the convergence by comparing the variances of different chains with the variances within chains. Large differences between these variances indicates nonconvergence. GRD can qualify whether the choice of the initial point largely affects the Markov chain with certain length or not. GRD monitors whether a Markov chain converges to a target posterior distribution because the Markov chain should forget where it starts once it converges. GRD is a very important diagnostic for MCMC in high-dimensional cases. When the high-dimensional target distribution is multimodal, the Markov chain is easy to be trapped around one local extremum of the distribution and may cause large error in most cases. Doing GRD on Markov chains initiated from different regions effectively show that whether these Markov chains have covered the entire sampling space.

The diagnostic can be done by running M Markov chains in parallel. Suppose we do GRD when the length of each chain is N. For a parameter θ, denote $\{\theta_{mt}\}^N_t = 1$ as the value of θ in the mth chain. Denote $\hat{\theta}_m$, $\hat{\sigma}^2_m$, and $\hat{\theta}$ respectively as the mean of θ in the mth chain, the variance of θ in the mth chain, and the overall mean of θ among all the chains. The between-chains variance B and within-chain variance W are given by

$$\frac{B}{N} = \frac{1}{M-1}\sum_{m=1}^{M}(\hat{\theta}_m - \hat{\theta})^2, \tag{D1}$$

$$W = \frac{1}{M(N-1)}\sum_{m=1}^{M}\sum_{t=1}^{N}(\theta_{mt} - \hat{\theta}_m)^2. \tag{D2}$$

The pooled posterior variance yields

$$\hat{V} = \frac{N-1}{N}W + \frac{M+1}{MN}B. \tag{D3}$$

In [82,83], the potential scale reduction factor is defined by

$$\hat{R} = \frac{\hat{V}}{W}, \tag{D4}$$

which compares the between-chains variance with the within-chain variance. If the Markov chains converge to the target distribution, then all the parameters θ should have their $\hat{R}$ close to one. Once the Markov chains converge, the sampling procedure can stop.

APPENDIX E: BENCHMARKS OF THE PINPOINT FINDER

In our saddle-point finder, the coarse finder roughly locates the saddle points. Therefore, the points fed to the pinpoint finder are close to the saddle points. In the region close to the saddle point, the action can be approximated by quadratic functions. As such, we use the quadratic function $-(\vec{x}\cdot\vec{x})$ to test the performance of our pinpoint finder.

TABLE XXVIII. The results of the benchmark.

Dimension	5	10	30	50	100	500	1000
Number of steps	227	227	227	227	227	227	227
Total time (seconds)	4.05	8.76	24.6	41.8	92.1	888	3852

TABLE XXIX. The results of the benchmark with respect to the initial distances.

Distances	1	5	10	20	50
Number of steps (10-dim)	227	242	248	255	264
Number of steps (50-dim)	227	242	248	255	264

To benchmark the pinpoint finder's performance in different dimensions, we run the pinpoint finder in 5, 10, 30, 50, 100, 500, and 1000 dimensional cases and measure the time for finding the saddle points with a numerical error less than 10^{-10} in the gradient of the action. The distances between the initial points and the saddle points are set to be 1. The results are shown in the Table XXVIII. The relation of the time versus the dimension is fitted as a second order function:

$$\text{time} = 32.5 - 0.316 \times \text{dim} + 0.00413 \times \text{dim}^2,$$

and shown in Fig. 5. This result shows that the time complexity for the pinpoint finder is in $\mathcal{O}(n^2)$ in n-dimensional cases. We also test how the distance between the initial points and the saddle points affects the time cost. In 10- and 50-dimensional cases, we test the pinpoint finder with different distances between the initial points and the saddle points. The results are shown in Table XXIX. From the results, we see that the number of steps is independent of the dimension. The logarithmic relation between the number of steps and the distance from the initial points to the saddle points is shown in Fig. 6.

These benchmarks show that our pinpoint finder is a polynomial algorithm. By Cobham's thesis [85], this algorithm is quick to solve in different dimensional cases. One thing to remark is that our pinpoint finder computes the components of Hessians and gradients in sequence. The finder would be faster than $\mathcal{O}(n^2)$, if one computes these components in parallel.

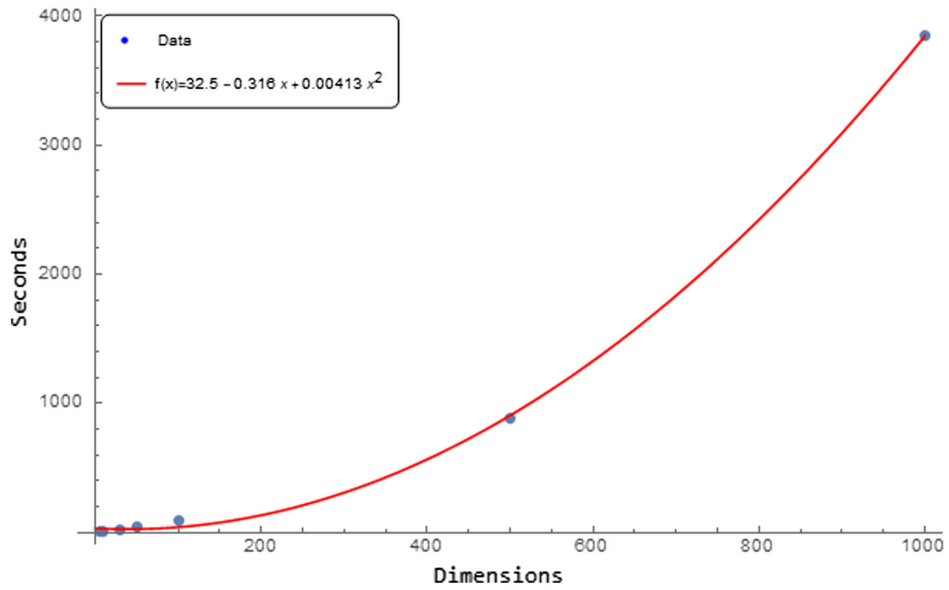

FIG. 5. The relation between the time costs and the dimensions.

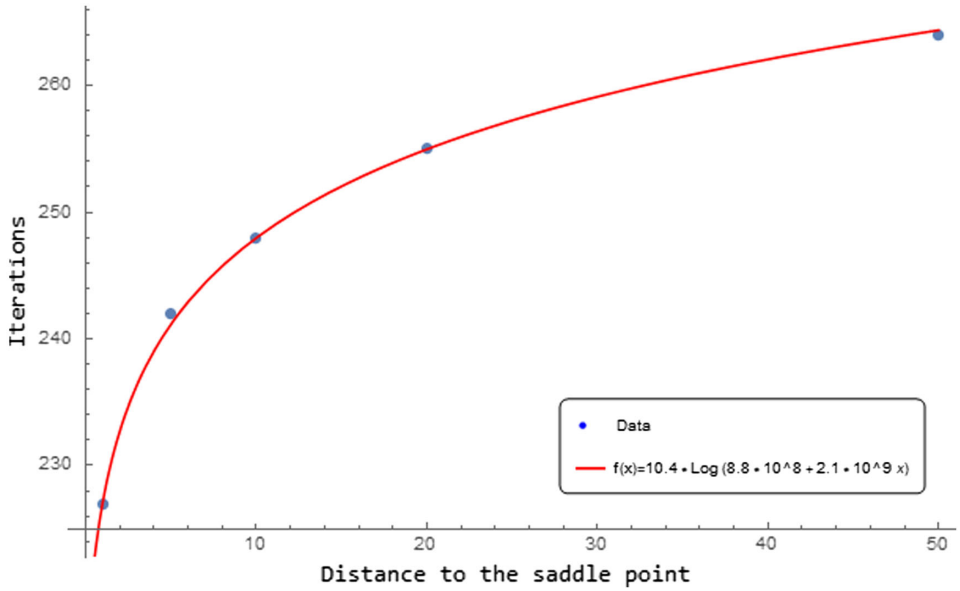

FIG. 6. The relation between the numbers of steps and the initial distances.

[1] Edward Witten, Analytic Continuation of Chern-Simons theory, AMS/IP Stud. Adv. Math. **50**, 347 (2011).
[2] Daniel Harlow, Jonathan Maltz, and Edward Witten, Analytic continuation of Liouville theory, J. High Energy Phys. 12 (2011) 071.
[3] Edward Witten, A new look at the path integral of quantum mechanics, arXiv:1009.6032.
[4] R. Balian and C. Bloch, Solution of the Schrödinger equation in terms of classical paths, Ann. Phys. (N.Y.) **85**, 514 (1974).
[5] E. Brézin, J.-C. Le Guillou, and J. Zinn-Justin, Perturbation theory at large order. II. Role of the vacuum instability, Phys. Rev. D **15**, 1558 (1977).
[6] Alan Lapedes and Emil Mottola, Complex path integrals and finite temperature, Nucl. Phys. **B203**, 58 (1982).
[7] I. I. Balitsky and A. V. Yung, Instanton molecular vacuum in $n = 1$ supersymmetric quantum mechanics, Nucl. Phys. **B274**, 475 (1986).
[8] Marco Cristoforetti, Francesco Di Renzo, and Luigi Scorzato, New approach to the sign problem in quantum field theories: High density QCD on a Lefschetz thimble, Phys. Rev. D **86**, 074506 (2012).
[9] H. Fujii, D. Honda, M. Kato, Y. Kikukawa, S. Komatsu, and T. Sano, Hybrid Monte Carlo on Lefschetz thimbles—A study of the residual sign problem, J. High Energy Phys. 10 (2013) 147.
[10] Gert Aarts, Lorenzo Bongiovanni, Erhard Seiler, and Denes Sexty, Some remarks on Lefschetz thimbles and complex Langevin dynamics, J. High Energy Phys. 10 (2014) 159.
[11] Hirotsugu Fujii, Syo Kamata, and Yoshio Kikukawa, Lefschetz thimble structure in one-dimensional lattice thirring model at finite density, J. High Energy Phys. 11 (2015) 078.
[12] Yuya Tanizaki, Yoshimasa Hidaka, and Tomoya Hayata, Lefschetz-thimble analysis of the sign problem in one-site fermion model, New J. Phys. **18**, 033002 (2016).
[13] Mithat Ünsal, Magnetic bion condensation: A new mechanism of confinement and mass gap in four dimensions, Phys. Rev. D **80**, 065001 (2009).
[14] Erich Poppitz, Thomas Schäfer, and Mithat Ünsal, Continuity, deconfinement, and (super) Yang-Mills theory, J. High Energy Phys. 10 (2012) 115.
[15] Erich Poppitz and Mithat Ünsal, Seiberg-Witten and "Polyakov-like" magnetic bion confinements are continuously connected, J. High Energy Phys. 07 (2011) 082.
[16] Alireza Behtash, Tin Sulejmanpasic, Thomas Schäfer, and Mithat Ünsal, Hidden Topological Angles in Path Integrals, Phys. Rev. Lett. **115**, 041601 (2015).
[17] Alireza Behtash, Gerald V. Dunne, Thomas Schäfer, Tin Sulejmanpasic, and Mithat Ünsal, Complexified Path Integrals, Exact Saddles, and Supersymmetry, Phys. Rev. Lett. **116**, 011601 (2016).
[18] Thomas Thiemann, *Modern Canonical Quantum General Relativity* (Cambridge University Press, Cambridge, England, 2007).
[19] Carlo Rovelli, *Quantum Gravity* (Cambridge University Press, Cambridge, England, 2004).

[20] Muxin Han, Yongge Ma, and Weiming Huang, Fundamental structure of loop quantum gravity, Int. J. Mod. Phys. D **16**, 1397 (2007).
[21] Muxin Han, Zichang Huang, Hongguang Liu, and Dongxue Qu, Complex critical points and curved geometries in four-dimensional Lorentzian spinfoam quantum gravity, Phys. Rev. D **106**, 044005 (2022).
[22] Frank Hellmann and Wojciech Kaminski, Geometric asymptotics for spin foam lattice gauge gravity on arbitrary triangulations, arXiv:1210.5276.
[23] Jonathan Steven Engle, Wojciech Kaminski, and José Ricardo Oliveira, Addendum to 'EPRL/FK asymptotics and the flatness problem', Classical Quantum Gravity **38**, 119401 (2021).
[24] Valentin Bonzom, Spin foam models for quantum gravity from lattice path integrals, Phys. Rev. D **80**, 064028 (2009).
[25] Muxin Han, On spinfoam models in large spin regime, Classical Quantum Gravity **31**, 015004 (2014).
[26] Francesco Gozzini, A high-performance code for EPRL spin foam amplitudes, Classical Quantum Gravity **38**, 225010 (2021).
[27] Jonathan Engle, Etera Livine, Roberto Pereira, and Carlo Rovelli, LQG vertex with finite Immirzi parameter, Nucl. Phys. **B799**, 136 (2008).
[28] C. Rovelli and F. Vidotto, *Covariant Loop Quantum Gravity: An Elementary Introduction to Quantum Gravity and Spinfoam Theory*, Cambridge Monographs on Mathematical Physics (Cambridge University Press, Cambridge, England, 2014).
[29] Muxin Han and Hongguang Liu, Analytic continuation of spin foam models (to be published).
[30] Muxin Han, Zichang Huang, Hongguang Liu, Dongxue Qu, and Yidun Wan, Spinfoam on a Lefschetz thimble: Markov Chain Monte Carlo computation of a Lorentzian spinfoam propagator, Phys. Rev. D **103**, 084026 (2021).
[31] Andrei Alexandru and Gökçe Başar, Paulo F. Bedaque, and Neill C. Warrington, Complex paths around the sign problem, Rev. Mod. Phys. **94**, 015006 (2022).
[32] Benjamin Bahr and Sebastian Steinhaus, Numerical Evidence for a Phase Transition in 4D Spin-Foam Quantum Gravity, Phys. Rev. Lett. **117**, 141302 (2016).
[33] Clement Delcamp and Bianca Dittrich, Towards a phase diagram for spin foams, Classical Quantum Gravity **34**, 225006 (2017).
[34] Inês Aniceto, Gökçe Başar, and Ricardo Schiappa, A primer on resurgent transseries and their asymptotics, Phys. Rep. **809**, 1 (2019).
[35] M. Cristoforetti, F. Di Renzo, A. Mukherjee, and L. Scorzato, Quantum field theories on the Lefschetz thimble, Proc. Sci. LATTICE2013 (**2014**) 197.
[36] Andrei Alexandru, Paulo F. Bedaque, Henry Lamm, and Scott Lawrence, Deep learning beyond Lefschetz thimbles, Phys. Rev. D **96**, 094505 (2017).
[37] Andrei Alexandru, Gökçe Basar, and Paulo Bedaque, Monte Carlo algorithm for simulating fermions on Lefschetz thimbles, Phys. Rev. D **93**, 014504 (2016).
[38] Andrei Alexandru, Gökçe Başar, Paulo F. Bedaque, Henry Lamm, and Scott Lawrence, Finite density QED_{1+1} near Lefschetz thimbles, Phys. Rev. D **98**, 034506 (2018).
[39] Andrei Alexandru, Gokce Basar, Paulo Bedaque, Gregory W. Ridgway, and Neill C. Warrington, Study of symmetry breaking in a relativistic Bose gas using the contraction algorithm, Phys. Rev. D **94**, 045017 (2016).
[40] Andrei Alexandru, Gokce Basar, Paulo F. Bedaque, Gregory W. Ridgway, and Neill C. Warrington, Monte Carlo calculations of the finite density Thirring model, Phys. Rev. D **95**, 014502 (2017).
[41] Job Feldbrugge, Ue-Li Pen, and Neil Turok, Oscillatory path integrals for radio astronomy, arXiv:1909.04632.
[42] Masafumi Fukuma and Nobuyuki Matsumoto, Worldvolume approach to the tempered Lefschetz thimble method, Prog. Theor. Exp. Phys. **2021**, 023B08 (2021).
[43] Minas Karamanis and Florian Beutler, Ensemble slice sampling, Stat. Comput. **31**, 61 (2021).
[44] Radford M. Neal, Slice sampling, Ann. Stat. **31**, 705 (2003).
[45] Antony Lewis and Sarah Bridle, Cosmological parameters from CMB and other data: A Monte Carlo approach, Phys. Rev. D **66**, 103511 (2002).
[46] Jesús Torrado and Antony Lewis, COBAYA: Code for Bayesian analysis of hierarchical physical models, J. Cosmol. Astropart. Phys. 05 (2021) 057.
[47] Laurent Freidel and Kirill Krasnov, A new spin foam model for 4d gravity, Classical Quantum Gravity **25**, 125018 (2008).
[48] Michael Reisenberger and Carlo Rovelli, Spin foams as Feynman diagrams, in *2001: A Relativistic Spacetime Odyssey. Proceedings, 25th Johns Hopkins Workshop on Problems in Particle Theory, Florence, Italy* (World Scientific, Hackensack, New Jersey, 2001), pp. 431–448.
[49] Alejandro Perez, Spin foam models for quantum gravity, Classical Quantum Gravity **20**, R43 (2003).
[50] Carlo Rovelli and Francesca Vidotto, *Covariant Loop Quantum Gravity an Elementary Introduction to Quantum Gravity and Spin Foam Theory* (Cambridge University Press, Cambridge, England, 2015), ISBN 978-1-107-06962-6.
[51] Carlo Rovelli and Lee Smolin, Spin networks and quantum gravity, Phys. Rev. D **52**, 5743 (1995).
[52] John W. Barrett and Louis Crane, Relativistic spin networks and quantum gravity, J. Math. Phys. (N.Y.) **39**, 3296 (1998).
[53] Roger Penrose, Angular momentum: An approach to combinatorial spacetime, in *Quantum Theory and Beyond: Essays and Discussions Arising from a Colloquium* (Cambridge University Presss, Cambridge, England, 1971), pp. 151–180.
[54] Muxin Han, Zichang Huang, and Antonia Zipfel, Spin foam propagator: A new perspective to include the cosmological constant, Phys. Rev. D **97**, 084055 (2018).
[55] Muxin Han, Zichang Huang, and Antonia Zipfel, Emergent four-dimensional linearized gravity from a spin foam model, Phys. Rev. D **100**, 024060 (2019).
[56] Emanuele Alesci, Graviton propagator as a tool to test spinfoam models, in *Proceedings of the 3rd Stueckelberg Workshop on Relativistic Field Theories, Italy, 2008* (Cambridge Scientific Publishers, Cambridge, 2009).
[57] Eugenio Bianchi and You Ding, Lorentzian spinfoam propagator, Phys. Rev. D **86**, 104040 (2012).

[58] Eugenio Bianchi, Elena Magliaro, and Claudio Perini, LQG propagator from the new spin foams, Nucl. Phys. **B822**, 245 (2009).
[59] Eugenio Bianchi, Leonardo Modesto, Carlo Rovelli, and Simone Speziale, Graviton propagator in loop quantum gravity, Classical Quantum Gravity **23**, 6989 (2006).
[60] Carlo Rovelli, Graviton Propagator from Background-Independent Quantum Gravity, Phys. Rev. Lett. **97**, 151301 (2006).
[61] Robert Oeckl, The general boundary approach to quantum gravity, arXiv:gr-qc/0312081.
[62] Robert Oeckl, General boundary quantum field theory: Foundations and probability interpretation, Adv. Theor. Math. Phys. **12**, 319 (2008).
[63] John W. Barrett, R. J. Dowdall, Winston J. Fairbairn, Frank Hellmann, and Roberto Pereira, Lorentzian spin foam amplitudes: Graphical calculus and asymptotics, Classical Quantum Gravity **27**, 165009 (2010).
[64] Muxin Han and Mingyi Zhang, Asymptotics of spinfoam amplitude on simplicial manifold: Lorentzian theory, Classical Quantum Gravity **30**, 165012 (2013).
[65] Muxin Han and Thomas Krajewski, Path integral representation of Lorentzian spinfoam model, asymptotics, and simplicial geometries, Classical Quantum Gravity **31**, 015009 (2014).
[66] John W. Barrett, R. J. Dowdall, Winston J. Fairbairn, Frank Hellmann, and Roberto Pereira, Lorentzian spin foam amplitudes: Graphical calculus and asymptotics, Classical Quantum Gravity **27**, 165009 (2010).
[67] John W. Barrett, R. J. Dowdall, Winston J. Fairbairn, Henrique Gomes, and Frank Hellmann, Asymptotic analysis of the EPRL four-simplex amplitude, J. Math. Phys. (N.Y.) **50**, 112504 (2009).
[68] Muxin Han and Hongguang Liu, Analytic continuation of spinfoam models, Phys. Rev. D **105**, 024012 (2022).
[69] Muxin Han and Mingyi Zhang, Spinfoams near a classical curvature singularity, Phys. Rev. D **94**, 104075 (2016).
[70] Muxin Han and Mingyi Zhang, Asymptotics of spinfoam amplitude on simplicial manifold: Euclidean theory, Classical Quantum Gravity **29**, 165004 (2012).
[71] Muxin Han, Einstein equation from covariant loop quantum gravity in semiclassical continuum limit, Phys. Rev. D **96**, 024047 (2017).
[72] Pietro Donà, Marco Fanizza, Giorgio Sarno, and Simone Speziale, Numerical study of the Lorentzian Engle-Pereira-Rovelli-Livine spin foam amplitude, Phys. Rev. D **100**, 106003 (2019).
[73] Muxin Han, Zichang Huang, Hongguang Liu, and Dongxue Qu, Numerical computations of next-to-leading order corrections in spinfoam large-j asymptotics, Phys. Rev. D **102**, 124010 (2020).
[74] Pietro Dona, Francesco Gozzini, and Giorgio Sarno, Numerical analysis of spin foam dynamics and the flatness problem, Phys. Rev. D **102**, 106003 (2020).
[75] John W. Barrett, Winston J. Fairbairn, and Frank Hellmann, Quantum gravity asymptotics from the SU(2) 15j symbol, Int. J. Mod. Phys. A **25**, 2897 (2010).
[76] Florian Conrady and Laurent Freidel, On the semiclassical limit of 4d spin foam models, Phys. Rev. D **78**, 104023 (2008).
[77] Muxin Han, On spinfoam models in large spin regime, Classical Quantum Gravity **31**, 015004 (2014).
[78] Wojciech Kaminski, Marcin Kisielowski, and Hanno Sahlmann, Asymptotic analysis of the EPRL model with timelike tetrahedra, Classical Quantum Gravity **35**, 135012 (2018).
[79] José Diogo Simão and Sebastian Steinhaus, Asymptotic analysis of spin-foams with timelike faces in a new parametrization, Phys. Rev. D **104**, 126001 (2021).
[80] Hongguang Liu and Muxin Han, Asymptotic analysis of spin foam amplitude with timelike triangles, Phys. Rev. D **99**, 084040 (2019).
[81] Huang Zichang, Spinfoam propagator code, https://gitee.com/ZCHuang1126/saddle-point-finder.git (2022).
[82] Andrew Gelman and Donald B. Rubin, Inference from iterative simulation using multiple sequences, Stat. Sci. **7**, 457 (1992).
[83] Stephen P. Brooks and Andrew Gelman, General methods for monitoring convergence of iterative simulations, J. Comput. Graph. Stat. **7**, 434 (1998).
[84] Nikolay Balov, Gelman–Rubin convergence diagnostic using multiple chains, https://blog.stata.com/2016/05/26/gelman-rubin-convergence-diagnostic-using-multiple-chains/#:~:text=The%20Gelman%E2%80%93Rubin%20diagnostic%20evaluates%20MCMC%20convergence%20by%20analyzing,parameter.%20Large%20differences%20between%20these%20variances%20indicate%20nonconvergence.
[85] Stephen A. Cook, Alan Cobham. The intrinsic computational difficulty of functions, logic, methodology and philosophy of science, in *Proceedings of the 1964 International Congress*, edited by Yehoshua Bar-Hillel, Studies in Logic and the Foundations of Mathematics (North-Holland Publishing Company, Amsterdam, 1965), pp. 24–30; J. Symb. Log. **34**, 657 (1970).